View metadata, citation and similar papers at core.ac.uk

brought to you by CORE

provided by Digital Repository @ Iowa State University

IOWA STATE UNIVERSITY
Digital Repository

Retrospective Theses and Dissertations

Iowa State University Capstones, Theses and Dissertations

1978

Determination of phase boundaries and diffusion parameters in tantalum hydrides by pulsed NMR

Phillip Allen Hornung
Iowa State University

Follow this and additional works at: https://lib.dr.iastate.edu/rtd

 Part of the Condensed Matter Physics Commons

Recommended Citation

Hornung, Phillip Allen, "Determination of phase boundaries and diffusion parameters in tantalum hydrides by pulsed NMR " (1978). *Retrospective Theses and Dissertations*. 6458.
https://lib.dr.iastate.edu/rtd/6458

This Dissertation is brought to you for free and open access by the Iowa State University Capstones, Theses and Dissertations at Iowa State University Digital Repository. It has been accepted for inclusion in Retrospective Theses and Dissertations by an authorized administrator of Iowa State University Digital Repository. For more information, please contact digirep@iastate.edu.

INFORMATION TO USERS

This material was produced from a microfilm copy of the original document. While the most advanced technological means to photograph and reproduce this document have been used, the quality is heavily dependent upon the quality of the original submitted.

The following explanation of techniques is provided to help you understand markings or patterns which may appear on this reproduction.

1. The sign or "target" for pages apparently lacking from the document photographed is "Missing Page(s)". If it was possible to obtain the missing page(s) or section, they are spliced into the film along with adjacent pages. This may have necessitated cutting thru an image and duplicating adjacent pages to insure you complete continuity.

2. When an image on the film is obliterated with a large round black mark, it is an indication that the photographer suspected that the copy may have moved during exposure and thus cause a blurred image. You will find a good image of the page in the adjacent frame.

3. When a map, drawing or chart, etc., was part of the material being photographed the photographer followed a definite method in "sectioning" the material. It is customary to begin photoing at the upper left hand corner of a large sheet and to continue photoing from left to right in equal sections with a small overlap. If necessary, sectioning is continued again – beginning below the first row and continuing on until complete.

4. The majority of users indicate that the textual content is of greatest value, however, a somewhat higher quality reproduction could be made from "photographs" if essential to the understanding of the dissertation. Silver prints of "photographs" may be ordered at additional charge by writing the Order Department, giving the catalog number, title, author and specific pages you wish reproduced.

5. PLEASE NOTE: Some pages may have indistinct print. Filmed as received.

University Microfilms International
300 North Zeeb Road
Ann Arbor, Michigan 48106 USA
St. John's Road, Tyler's Green
High Wycombe, Bucks, England HP10 8HR

7813231

HORNUNG, PHILLIP ALLEN
DETERMINATION OF PHASE BOUNDARIES AND DIFFUSION PARAMETERS IN TANTALUM-HYDRIDES BY PULSED NMR.

IOWA STATE UNIVERSITY, PH.D., 1978

University Microfilms International 300 N. ZEEB ROAD, ANN ARBOR, MI 48106

Determination of phase boundaries and diffusion parameters in tantalum hydrides by pulsed NMR

by

Phillip Allen Hornung

A Dissertation Submitted to the

Graduate Faculty in Partial Fulfillment of

The Requirements for the Degree of

DOCTOR OF PHILOSOPHY

Department: Physics
Major: Solid State Physics

Approved:

Signature was redacted for privacy.

In Charge of Major Work

Signature was redacted for privacy.

For the Major Department

Signature was redacted for privacy.

For the Graduate College

Iowa State University
Ames, Iowa

1978

TABLE OF CONTENTS

CHAPTER I. INTRODUCTION

Both from a purely scientific and a technological viewpoint, the introduction of hydrogen into a metal lattice leads to interesting properties. Hydrogen, the lightest atom, can serve as an extreme case for the study of interstitial alloys. Metal-hydrogen systems are of immense practical importance with many applications. A few of these are storage and transport for hydrogen fuel cells and combustion engines, and fusion reactor vessels. The embrittlement that interstitial hydrogen causes is of great concern in industrial chemical processes, reactor vessel wall construction, and aircraft fatigue analysis. In basic scientific terms, it poses questions about the electronic, structural, and diffusive character of the alloy. Their solutions may eventually lead to explanations of the wide range of hydrogen solubility, its capability to embrittle a host lattice, and the difficulties encountered in loading a sample with hydrogen. Consequently, much work has been done to study the internal hydrogen motion, the structure and its transitions, and the electronic properties of these metal hydrogen systems.

In particular, the hydrides of the group Vb transition metals, tantalum, niobium, and vanadium, have been the subject of intense recent study by a variety of techniques. These metals exhibit quite similar properties upon the absorption of hydrogen into the lattice. They belong to the class of so-called exothermic occluders of hydrogen and in them hydrogen has the fastest diffusion rates found in solids (1). At room temperature, the diffusion of hydrogen in these materials is comparable to the diffusion of air molecules. The hydrogen in its metal host

expands the lattice slightly and occupies either an octahedral or tetrahedral interstitial site in an approximately body-centered cubic (bcc) cell. The hydrogen exists in an atomic, not molecular, state and forms a bond most similar to that between atoms in a metal-metal alloy.

The electronic properties of metal hydrides are at the center of the greatest controversy. The hydrogen's electron vastly complicates the entire question. Solubility arguments and some calculations (2) indicate that the hydrogen may be heavily screened by attracting another electron from the metal's conduction band. On the other hand, nuclear magnetic resonance data (3) and Compton scattering data (4) indicate that the hydrogen electron is given up to the conduction band. The electronic properties also are the principal factor in determining the hydrogen solubility.

The electronic properties of these materials have been calculated using Madelung (5), bond (2), and band (6) theories. Certainly, the most believable of these are Switendick's band computations. Band theories are sensitive to the crystalline structure and do not, as other calculations do, assume the nature of the crystal beforehand. For the bcc metal monohydrides, Switendick finds only a minor effect, that is, a lowered (in energy) s-band near the tetrahedral site. This seems to indicate that a combination of both of the simple arguments may be correct. To the extent that an almost filled s-band gains electrons because of its lowered energy, the interstitial hydrogen may gain some effective

additional screening. Remaining electrons would increase the density of electrons at the Fermi surface slightly, giving an increased conduction electron density.

The crystalline structure of these alloys is an interesting combination of ordering and structural phase differences (7). A discussion of the structures presently established for tantalum is presented in the next chapter. Briefly, the Vb metal hydrides are body centered cubic in their high temperature phase with the addition of interstitial hydrogen expanding the lattice parameter slightly. The hydrogen diffuses rapidly throughout the structure, and randomly occupies tetrahedral sites in niobium and tantalum, and both tetrahedral and octahedral sites in vanadium. As the temperature is lowered, the structure distorts slightly to face centered orthorhombic. The changes in lattice parameter and angle are less than one percent. Additionally, the hydrogen begins to occupy ordered arrangements of interstitial sites, becoming more highly ordered at lower temperatures.

Finally, a major portion of the interest in the hydrides concerns the translational motion of the hydrogen. Measurements on the parameter of interest, the diffusion coefficient, are quite difficult. Most of the macroscopic techniques make use of a measurement of the number flux of hydrogen driven by a concentration gradient. However, the results are ambiguous when the diffusion rates depend upon concentration. The technique described in this thesis avoids this difficulty, but provides only information on the jump rate of hydrogen and not the diffusion coefficient directly. Usually modeled as having an Arhennius dependence

upon an activation energy, the jump rate is proportional to the diffusion coefficient. The typical value for the activation energy for hydrogen diffusion in tantalum is 0.140 electron volts per atom. There has also been a great deal of discussion regarding the systematics of the activation energy with hydrogen concentration.

Nuclear magnetic resonance experiments yield information about the three major categories given above and provide an interesting insight into the metal hydrides. In particular, nuclear magnetic resonance can be quite sensitive to small changes in structure and to diffusive motions. This thesis explores some arguments as to the nature of the structure and changes in the motions of hydrogen in tantalum.

CHAPTER II. THE TANTALUM HYDRIDE PHASES

At this writing, the phase diagram has been partially established for the tantalum hydride system. As many as seven phases have been postulated. Schober and Carl (8) have produced the most complete survey of the phase character. The phase diagram resulting from their work is presented as Figure 1. This figure will be extensively used, but other sources will also be cited. In particular, the boundaries are assigned solely on the basis of differential thermal analysis measurements, whereas the other techniques such as neutron, x-ray, and electron diffraction must be used to identify the structure. The phases for which the structures have been identified are α, β, δ, and ζ, and the γ and ϵ phase boundaries have been found. The identifications used here are those of Schober and Carl and, differing from the rest of the literature, they have assigned ζ to the Ta_4H_3 phase and used γ (used by other sources for Ta_4H_3) for a different structure centered on 80 atom percent.

α Phase

These hydrides are usually only small modifications of the host structure as the hydrogens occupy interstitial positions. Tantalum metal's body centered cubic structure remains in the high temperature region ($T > 100^{\circ}C$) until the hydrogen dissociates at about $500^{\circ}C$ (9). The hydrogen is free to jump between any of the tetrahedral sites (see Figure 2). This structure is commonly denoted as the solid solution or

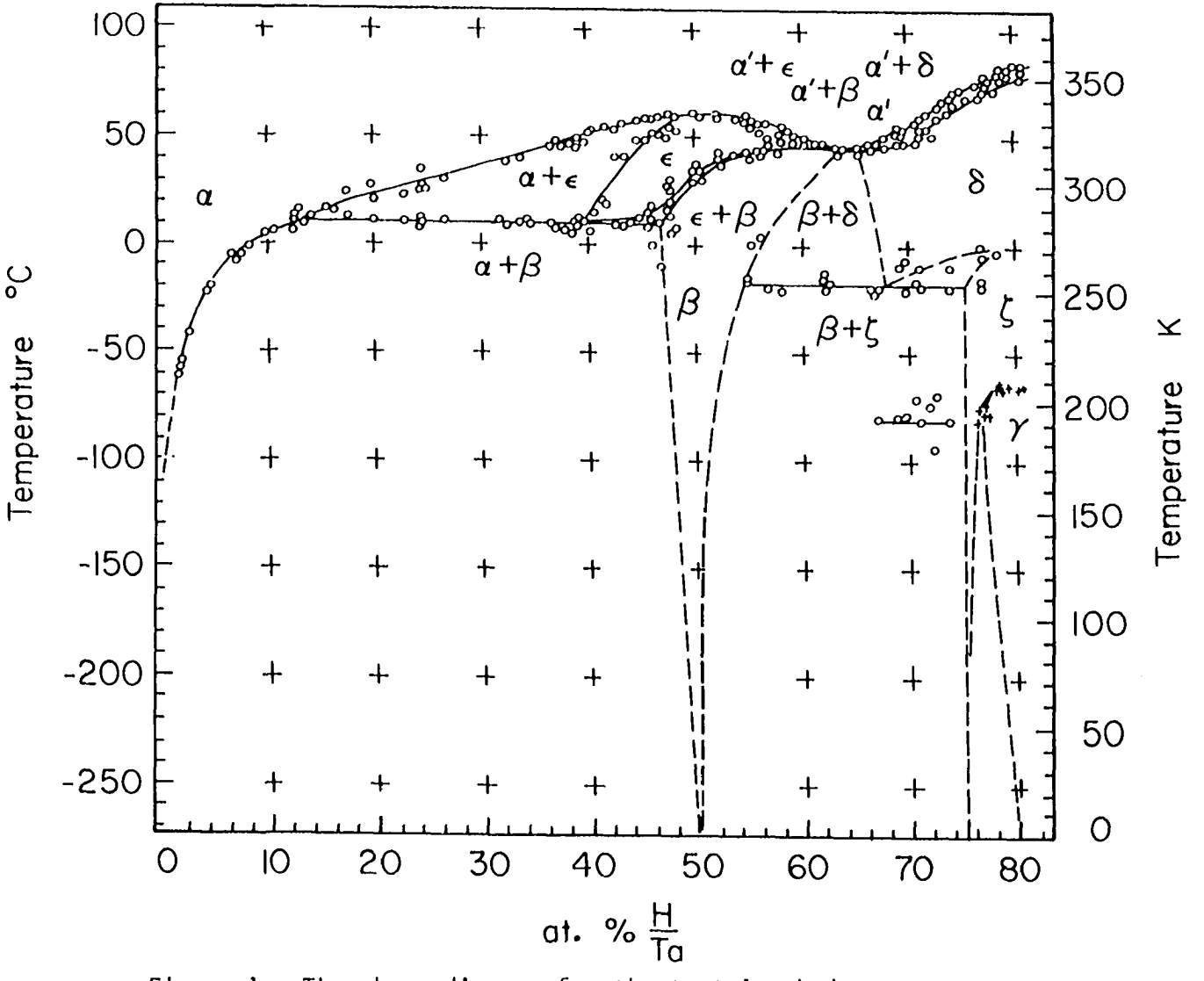

Figure 1. The phase diagram for the tantalum-hydrogen system was determined by Schober and Carl (8) by differential thermal analysis.

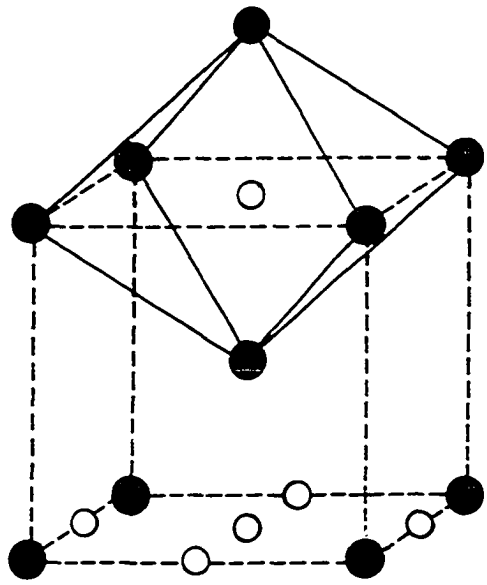

OCTAHEDRAL SITES
IN A BCC LATTICE

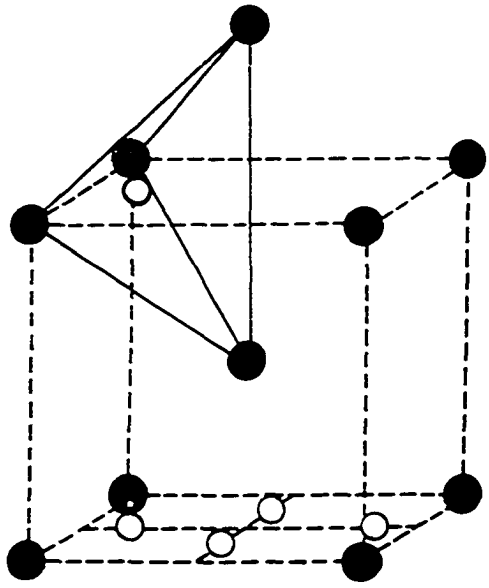

TETRAHEDRAL SITES
IN A BCC LATTICE

Figure 2. A body centered cubic lattice has two kinds of interstitial sites.

α phase. The principal effect of the hydrogen in this phase is to increase the lattice parameters with increasing hydrogen content (10).

The Ordered Phases

As the temperature is reduced, the bcc lattice distorts into a non-cubic symmetry with changes in one angle of 0.62° and in the lattice parameters of approximately one percent (11). These structural changes modify the bcc cell, making the symmetry either tetragonal or orthorhombic. These lower symmetry phases differ from each other by lattice parameter changes with hydrogen concentration and hydrogen ordering within the unit cell. The distortion has a further effect which is much more pronounced. It limits the hydrogen occupation to interstitial sites lying in a plane paralleling a body diagonal. Figure 3 shows this plane in the new face centered orthorhombic cell. Deuteron magnetic resonance (12) clearly shows that the hydrogen (deuterium) samples only the four sites of the unit cell in this plane at temperatures below the phase transition and all tetrahedral sites above it in the α phase. This plane then becomes central to the discussion of the ordered phases.

δ Phase

At full stoichemetry, the δ phase (TaH or TaD structure) has all of the hydrogen sites in this plane filled as is shown in Figure 4c. The arrows in the diagram show the displacement direction of the tantalum in the distorted structure. Departures from stoichiometry are achieved by vacating hydrogen atoms from the available tetrahedral sites

Figure 3. The slight distortion of the body centered cubic lattice changes the unit cell to face centered orthorhombic and restricts hydrogen occupation to tetrahedral sites upon the shaded plane. The original body centered cubic lattice can be visualized by noting that the left front face of the face centered orthorhombic structure contains a body diagonal of the original BCC structure. This figure was adapted from T. Schober and U. Linke (13a).

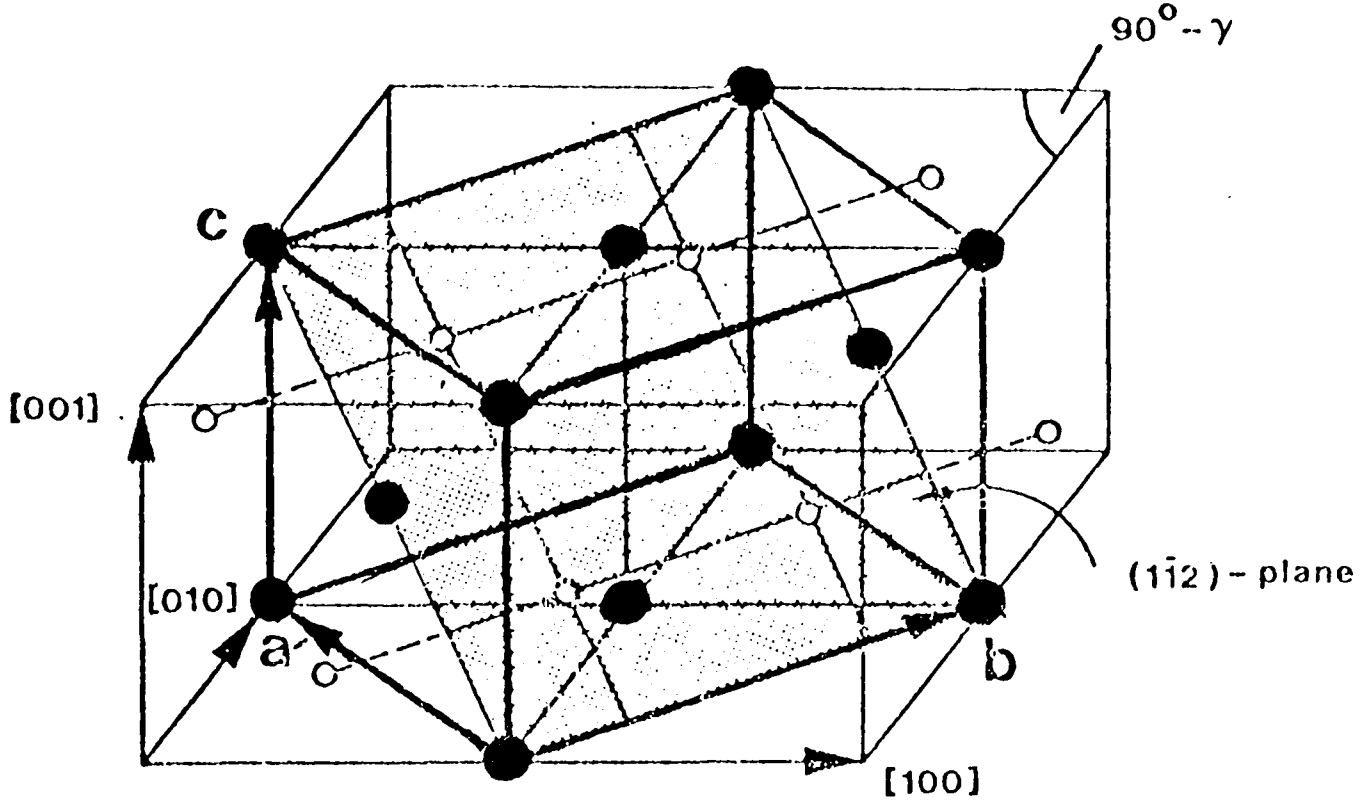

● = Ta

o = H

Figure 4. Hydrogen atoms only occupy tetrahedral sites within the plane shown here when the lattice transforms into the face centered orthorhombic structure. Depending upon the hydrogen concentration and the temperature, different ordered arrangements of the hydrogen atoms occur. Figure 4a shows the lattice for H/Ta = 0.50, with the hydrogen sublattice explicitly displayed below it. Figure 4b illustrates the longest range ordered detected at H/Ta = 0.75. The arrows in 4a and 4b show the directions of the slight distortions in the structures. Figure 4c has all the sites within the plane occupied in the H/Ta = 1.00 composition. The original BCC cell is outlined to the right. In each case, the hydrogen sublattice changes, increasing by a factor of two in spatial repeat distance in the order H/Ta = 1.00, 0.50, and 0.75. The Figure was adapted from Asano et al. (13b).

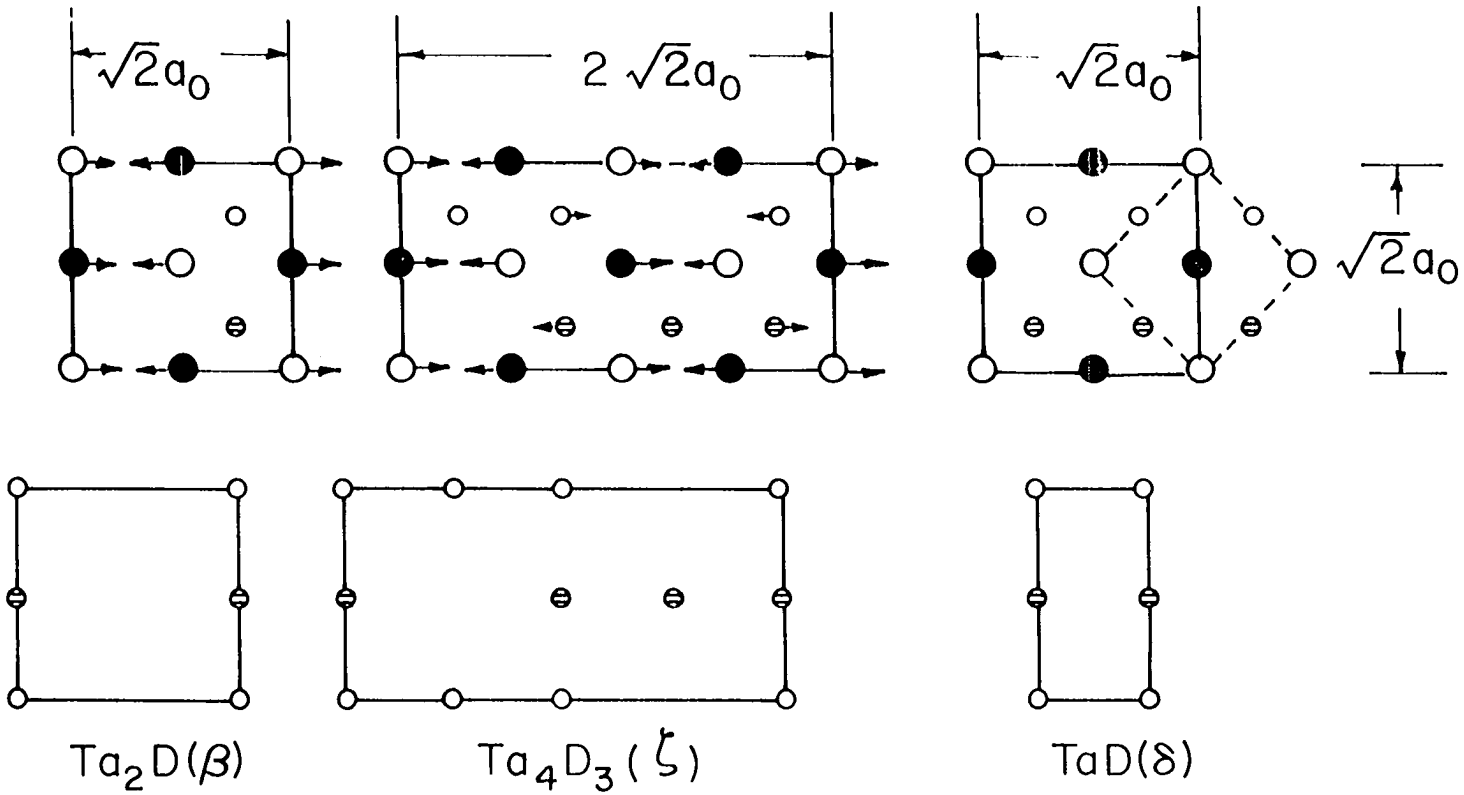

4a 4b 4c

randomly from the four sites (9). More precisely, this can only be said to involve the removal randomly of pairs of sites, since, for neutron diffraction, there are two pairs of reflections, a sites at $(\frac{1}{4}\ \frac{1}{4}\ \frac{1}{4})$ and $(\frac{3}{4}\ \frac{3}{4}\ \frac{3}{4})$ and b sites at $(\frac{3}{4}\ \frac{1}{4}\ \frac{1}{4})$ and $(\frac{1}{4}\ \frac{3}{4}\ \frac{3}{4})$.

β Phase

The next simplest ordered structure is the β phase at composition Ta_2H shown in Figure 4a. In contrast to the δ phase, one notes that the superlattice of hydrogen or deuterium now has twice the spatial repeat distance that the δ phase superlattice has. Somenkov et al. (9) further comments that the structure has uniformly maximized the hydrogen-hydrogen distance by retaining one each of the a and b sites mentioned previously. He postulates that this is to ensure the most uniform charge density throughout the lattice. The hydrogen tends to further distort the lattice by decreasing the distance between rows of tantalum atoms which have no hydrogen atoms between them and increasing that same distance when the sites are filled (14). The arrows in Figure 4a show this distortion. The hydrogen-rich and hydrogen-poor sites each form planes parallel to the c axis ($1\bar{1}0$ planes relative to the distorted bcc cell).

In the β phase, deviations from stoichiometry are achieved by filling randomly the remaining tetrahedral sites in the plane or by removing a hydrogen from one of the filled sites for lower concentrations (13b). This phase exists as a single phase only in a very limited composition range.

ζ Phase

When the hydrogen concentration is in the 75 atom percent range, the Ta_4H_3 or ζ phase forms at about 250K. This has further ordering in the occupied interstitial plane as in shown in Figure 4b. Neutron diffraction work (15) revealed this structure which has a very distinct set of superlattice reflections. In much of the previous literature this phase was labeled γ; here the convention of Schober and Carl is used since theirs is the most complete work at this time.

ε and γ Phases

Although boundaries for both the ε and γ phases have been established, the structures of the two phases remain unknown at this writing. The ε phase is presumed to be tetragonal (8) and metallographic studies show its existence conclusively. The γ phase is clearly a further ordering of the ζ phase although its ordering arrangement is not clear. The ordering is postulated to form a Ta_5H_4 structure since the peak in the phase diagram falls between 80 and 82 atomic percent.

Summary

Schober and Carl have obtained excellent agreement in their DTA and metallographic work with much of the previous work. With the large number of single crystal samples studied, they have established most of the phase boundaries previously open to discussion. Much of the quality of their measurement stems from the use of single crystals rather than powder. This eliminates the problem of imhomogenity of hydrogen concen-

tration within the sample. In contrast to Schober and Carl's work, Asano et al. (16) made a DTA study on powdered samples with quite different and inconsistent results. When metal is hydrided, surface impurities such as oxygen and nitrogen control the rate of hydrogen absorption into the sample. If this sample is already a powder, the hydrogen absorbed into a particle may vary from particle to particle. A great deal of the confusion in the literature stems from this fact. In the higher concentration regions, this problem becomes much more critical. At present, Schober and Carl have the only work on tantalum hydrides using single crystals. The DTA studies do not however provide structural determinations so that only the boundaries are actually found. Since the neutron diffraction studies use powder samples, the nature of the high concentration-low temperature phases remains uncertain.

The restriction of hydrogen to the ordering plane and its preferential occupation of sites within the plane form one of the most interesting problems in hydride structures. Somenkov (17) states the problem in the following fashion: As the temperature goes to zero, random occupation of sites is thermodynamically unstable since the configurational entropy does not also go to zero. Therefore, the configuration may go to either two separate low ordering phases or to a single highly ordered phase. Both of these alternatives have been observed; the first in the low concentration region for NbH (18) and the second in the work of Somenkov et al. (15) and Asano (13) on $TaH_{0.75}$.

In the higher ordering case, Somenkov notes that the ordering follows a step-wise branching scheme. The first step is an order-disorder

transition ($\alpha \rightarrow \delta$) which has four possible reciprocal lattice vectors associated with the tetrahedral sites of the bcc cell. The branching scheme postulates several possibilities for each reciprocal vector. Each succeeding step has half of one of these vectors as its characteristic of a more highly ordered phase. This is equivalent to doubling the spatial repeat distance along some axis. It should be further noted that these patterns are not unique, i.e. that although tantalum and niobium both form a Me_4H_3 structure, they form it on the basis of differing reciprocal vectors. This doubling for the tantalum hydride case is most obvious from Figure 4.

Ultimately, the ordering of these structures implies that there must be inequivalent sites based on the branching scheme, or on some similar one. The formation of still more ordered compounds may be limited by kinetic considerations, but these have not yet been seen.

CHAPTER III. DIFFUSION

The mobility of atoms in solids gives rise to macroscopic transport of these atoms when a concentration gradient exists across the specimen. If c is the concentration and $\vec{J}$ the vector flux of the atoms through a unit area perpendicular to the gradient, then $\vec{J}$ is given by Fick's first law (19), $\vec{J} = - D\vec{\nabla}c$. The diffusion coefficient, D lumps all of the microscopic details into one constant of proportionality. When Fick's first law describes the motion of atoms in a mono-atomic lattice, such as lithium atoms in lithium metal, the process is called self-diffusion. By contrast, in the case of interstitial diffusion in which an interstitial species moves through the lattice, the diffusion coefficient may and often does depend upon concentration. When this situation occurs, the diffusion coefficient can only be measured rigorously at small concentration gradients.

The diffusion process itself is modeled in a number of different ways but, usually, the simplest model is nearly as appropriate as the most complex. For purposes of analyzing nuclear magnetic resonance data, the Bloembergen, Purcell, and Pound (BPP) (20) theory is well-accepted. Torrey (21) developed a more elaborate theory which is, for most purposes, less useful than BPP theory as will be discussed in the analysis section. Abragam (22) discusses both of these models in some detail.

An isotropic model of diffusion which has had notable success in the cases of liquids and interstitial solid solutions is used. This

model postulates a simple Arhennius behavior based upon the assumption of a single correlation time for the atomic jump. The diffusion coefficient is given by

$$D = \frac{1}{6} \frac{\langle \lambda \rangle^2}{\tau_c} , \qquad 1$$

where $\langle \lambda \rangle^2$ is a squared average jump distance, and τ_c is the correlation time. The correlation function G(t) is the probability of an atom remaining in its local environment for a time t, and one model of the correlation function is

$$G(t) = e^{-t/\tau_c}. \qquad 2$$

The correlation time may be more simply regarded as just the mean residence time of an atom in a specific site. The actual jump is considered to occur instantaneously. The correlation time and its inverse, the jump frequency, are further modeled as

$$\nu = \frac{1}{\tau_c} = \nu_o g p \exp\{-E_a/kT\}, \qquad 3$$

where ν_o is the vibrational frequency of the atom at the bottom of the potential well, g the number of available jump sites, p the probability that a neighboring site is unoccupied, and E_a the activation energy associated with each jump. This model thus contains the Arrhenius behavior parameterized by E_a which may be thought of as the energy needed to physically open the lattice enough for the atomic jump to take place. Unlike the case of self-diffusion on a mono-atomic lattice (e.g., lithium metal), no energy is required to create the vacant site to which the jump occurs.

For a bcc lattice, it has been shown by Beshers (23) that the occupancy and jump paths depend upon the relative size of the interstitial and the elasticity of the lattice. With light atom interstitials and a heavy atom lattice as in the tantalum hydrides, this certainly appears to be true. Jumps are then by two kinds: tetrahedral-tetrahedral (tt) or tetrahedral-octahedral-tetrahedral (tot). (See Figure 2). The jumps have very different path lengths and may have different activation energies.

The principal use of nuclear magnetic resonance for diffusion measurements is to determine the frequency of the jumping motion ν. This frequency or its inverse τ_c, the correlation time, can be related to specific temperature dependences of the spin system's relaxation mechanisms, and, from that, the activation energy of the jumping motion.

CHAPTER IV. NUCLEAR MAGNETIC RELAXATION

Nuclear magnetic resonance (NMR) furnishes a very sensitive and non-disruptive probe of the local electronic and magnetic environment of the resonant nuclear species in a substance. A variety of measurements are available to determine specific environmental effects. For motional and structural problems, the pattern of the resonance versus frequency or the complementary measurement of the relaxation times are the most commonly used. In addition, the results may provide insights into phase transitions, tunneling effects, and electronic behavior.

Semi-Classical Model

These measurements are readily understood in terms of the behavior of a classical magnetization vector in an applied magnetic field (24). The energy of such a vector depends on its orientation

$$E = -\vec{M}\cdot\vec{H}, \qquad 4$$

where $\vec{M}$ and $\vec{H}$ are the magnetization and applied field vectors respectively. For convenience, the static strong applied field is taken to be along the z-axis and the remaining magnetic fields are contained in $\vec{H}_i$, so that

$$\vec{H} = H_o\hat{k} + \vec{H}_i \ .$$

The classical time dependence of $\vec{M}$ derives from the torque equation,

$$\frac{d\vec{M}}{dt} = \gamma\vec{M} \times \vec{H} \ , \qquad 5$$

where γ is the gyromagnetic ratio relating the angular momentum to the

magnetization. If $\vec{H}$ consisted only of the static magnetic field, then the motion would be a steady precession about the z-axis. By transforming the calculation into the rotating frame,

$$\left(\frac{d\vec{M}}{dt}\right)_{rot} = \gamma\vec{M} \times H_o\hat{k} + \vec{M}\times\vec{\omega} + \gamma\vec{M} \times \vec{H}_i$$

the precession is eliminated if the resonant frequency $\vec{\omega}$ has the value

$$\vec{\omega} = -\gamma H_o \hat{k}, \qquad 6$$

so that

$$\frac{\partial\vec{M}}{\partial t} = \gamma\vec{M} \times \vec{H}_i \ . \qquad 7$$

All quantities are now understood transformed to the rotating frame.

Although the z-axis is the same in both the rotating and laboratory frames, the coordinate axes in the rotating frame are precessing at angular frequency $\vec{\omega}$ compared to the laboratory frame. This leads to the interesting situation that recovery of the magnetization to equilibrium along the z-axis is different from recovery in the xy plane. From equation 7, one sees that static or stationary fields in the rotating frame will be the most effective in producing changes of $\vec{M}$. A stationary field in the rotating frame appears to rotate at the resonant frequency in the laboratory frame as far as vectors in the xy plane are concerned. When these facts are combined with use of the torque equation, one notes that changes in M_z result from fluctuating or oscillatory fields in the laboratory xy plane, which are most effective if the fluctuations occur at the resonant frequency. By contrast, changes in M_x and M_y arise both from stationary z-direction fields at zero frequency

in the laboratory frame and from fields in the xy plane rotating at the resonant frequency again in the laboratory frame. Therefore, as expected, very different physical situations exist in the two cases. The evolution of M_z is characterized by an exponential decay with a time constant T_1, the spin-lattice relaxation time. Relaxation in the xy plane is called spin-spin relaxation and is characterized by a time T_2. An elementary model of such a system is contained in the Bloch Equations (25)

$$\frac{dM_z}{dt} = \frac{M_o - M_z}{T_1} \qquad 8a$$

$$\frac{d(M_x \text{ or } M_y)}{dt} = - \frac{(M_x \text{ or } M_y)}{T_2} \qquad 8b$$

It is also apparent from equation 4 that when M_z varies, the energy of the spin system changes. Fluctuations in M_x or M_y do not change the total energy of the spin system. This will become more evident in the quantum mechanical treatment.

This mechanical model presents a good physical picture but has serious drawbacks for any real predictive calculation. Since the quantized nature of the nuclear spin is fundamental to the phenomenon of magnetic resonance, it is necessary to use quantum theory to evaluate T_1 and T_2 for various physical situations.

Quantum Treatment

A nucleus has a spin quantum number I and a gyromagnetic ratio γ which are fixed for any one isotope. As a result of this, a weak magnetic moment $\vec{\mu}$ appears

$$\vec{\mu} = \gamma\hbar\vec{I} \ .$$

The magnetic moment has a magnitude

$$|\vec{\mu}| = \gamma\hbar(I\{I+1\})^{\frac{1}{2}} \ ,$$

with a quantized polarization number m which takes on values from -I to I in unit steps. Along any axis of quantization, say the z-axis,

$$\mu_z = \gamma\hbar m \ ,$$

with the remaining components of $\vec{\mu}$ forming a cone of possible orientations around the z-axis with an angle Θ

$$\Theta = \cos^{-1} m(I[I+1])^{-\frac{1}{2}}.$$

The energy of such a system in an applied field H_o (which determines the axis of quantization) is the magnetic dipole energy

$$E = -\hbar\gamma H_o m, \qquad 9$$

while the off-axis components precess about the z-axis at an angular frequency, ω

$$\omega = \gamma H_o \ , \qquad 10$$

known as the resonance or Larmor frequency.

When an ensemble of these spins is in equilibrium, no phase correlation exists between the precessing components of the spins. Since the energy level splittings are small compared to the thermal energy, a Boltzmann distribution describes the population of the energy levels which the static field produces. The small surplus number of nuclei in each succeedingly lower energy state produces a net magnetic moment parallel to the field, and this is the measurable quantity in NMR experiments.

For spin $\frac{1}{2}$ nuclei such as hydrogen, there is only the dipole-dipole interaction present, but for other nuclei with spin ≥ 1, electric quadrupole interactions complicate the problem. The discussion that follows is condensed from the thorough reference by Abragam (22), and where other sources are used they will be noted. The discussion follows the following sequence; first, the calculation of the ensemble behavior is described briefly, a series of simplifications based on spin systems are introduced, the dipole-dipole interaction is used to get an explicit formula, and, finally, the case of motion of the spins is analyzed in the context of the dipolar interaction.

To determine behavior of an ensemble of spins at a finite temperature, the density matrix formalism is most suitable and useful. Although it is not necessary to compute the matrix itself, manipulations with it yield the results desired. The expectation value of an ensemble observable Q is given by the trace or diagonal sum of the density matrix, ρ, multiplied by Q.

$$\langle Q \rangle = \mathrm{tr}[\rho Q] \ . \qquad 11$$

The time evolution of the density matrix is given by the commutation relation (25)

$$i \frac{\partial \rho}{dt} = [H,\rho] \ . \qquad 12$$

The interaction picture of quantum mechanics (26) is convenient for the calculation. In the interaction scheme, a variable's behavior in a steady-state situation is implicitly written into the density matrix while the interaction Hamiltonian is used to compute explicitly the transient time evolution. The change to the interaction picture

is analogous to transforming into the rotating frame in the classical model. The total Hamiltonian $\mathcal{H}$ is divided into steady-state parts $\mathfrak{F}$ containing only lattice coordinate operators and the applied field portion $\mathcal{H}_o$, and a non-steady state interaction term $\mathcal{H}_i$, as follows

$$\mathcal{H} = \mathcal{H}_o + \mathfrak{F} + \mathcal{H}_i .$$

The operators change to the interaction picture according to

$$Q^*(t) = e^{i[\mathcal{H}_o+\mathfrak{F}]t/\hbar} \, Q \, e^{-i[\mathcal{H}_o+\mathfrak{F}]t/\hbar} , \qquad 13$$

where the star denotes an interaction picture variable.

The density matrix in this representation evolves as

$$i \frac{d\rho^*}{dt} = -[\mathcal{H}_i^*, \rho^*(t)] . \qquad 14$$

Integrating equation 14, and substituting the result into the right hand side of the original equation 14, the time dependence of the spin density matrix is,

$$\frac{d(\rho^*(t) - \rho^*(o))}{dt} = - \int_o^t d\tau [\mathcal{H}_i^*(t), [\mathcal{H}_i^*(t-\tau), \rho^*(o)]] , \qquad 15$$

noting that setting t=o in the rightmost density matrix effectively ignores higher order commutators.

The interaction Hamiltonian can be written as a sum of products of lattice coordinate and spin operators, F^q and A^q respectively,

$$\mathcal{H}_i = \sum_q F^q A^q . \qquad 16$$

The particular form depends upon the appropriate Hamiltonian. Converting

the product to the interaction representation gives

$$\mathcal{H}_1^* = \sum_q F^q(t)\, e^{i\mathcal{H}_o t/\hbar} A^q e^{-i\mathcal{H}_o t/\hbar} \qquad 17$$

Although $\mathcal{F}$ and $\mathcal{H}_o$, and $\underline{\mathcal{F}}$ and A commute, $\mathcal{H}_1$ and A^q do not commute so that the lattice time dependence can be written normally. With the substitution of 17 into 15, the time evolution becomes

$$\frac{d(\rho^*(t)-\rho^*(o))}{dt} = -\int_o^t \sum_{qq'} d\tau\, F^q(t)F^q(t-\tau)$$

$$\times [A^{*q},[A^{*q'}, \rho^*(o)]] \qquad 18$$

The discussion is now simplified to the interaction between two spins labeled I and S which are magnetically coupled. Only paired interactions are considered and the lattice sum of such interactions is the total interaction. Then the F and A operators are explicitly

$$F^o = (1-3\cos^2\theta)/r^3 \qquad A^o = \alpha[-\tfrac{2}{3} I_z S_z + \tfrac{1}{6}(I^+S^- + I^-S^+)]$$

$$F^{\pm 1} = \sin\theta\cos\theta\, e^{\mp i\varphi}/r^3 \qquad A^{\pm 1} = \alpha[I_z S^{\pm} + S_z I^{\pm}]$$

$$F^{\pm 2} = \sin^2\theta\, e^{\mp i2\varphi}/r^3 \qquad A^{\pm 2} = \frac{\alpha}{2} I^{\pm} S^{\pm}, \qquad 19$$

where $\alpha = \dfrac{3\hbar^2\gamma_I\gamma_S}{2}$, $I^{\pm} = I_x \pm iI_y$ (the spin raising and lowering operators), and r,θ,φ are the coordinates of the displacement vector relative to the applied field.

Using this form of the interaction Hamiltonian, the calculation of the time evolution of the spin density matrix is facilitated by means of a series of observations. First, the spherical harmonics (F functions) are orthogonal. Then in addition, any time dependence should only

enter as the difference between two times and not referenced to a particular time origin. If $G^q(\tau)$ expresses the time relation between two states, then a sum over lattice states (tr_f) results in

$$tr_f\ F^q(t)\ F^{q'}(t-\tau) = \delta_{q-q'}\ G^q(\tau) \qquad 20$$

where $\delta_{q-q'}$ is the Kronecker delta function. The function $G^q(t)$ is the time correlation function, and its fourier transform $J^q(\omega)$ is the spectral density function defined by

$$J^q(\omega) = \int_{-\infty}^{\infty} G^q(t)e^{-i\omega t}dt. \qquad 21$$

Because the lattice operators of the density matrix are diagonal with respect to the spin operators, and the calculation only seeks to predict the spin system behavior, the lattice states based on the $\mathfrak{F}$ Hamiltonian can be separated out and removed from the calculation altogether. This assertion only holds when the specific heat of the lattice is much greater than that of the spin system, so the lattice retains thermal equilibrium independent of the spin system's configurations. Except at very low temperatures, this is nearly always the case. The assumption is stated as

$$\sigma = tr_f\ \rho. \qquad 22$$

Substituting these statements into equation 18 and taking the trace over the lattice states yields

$$\frac{d}{dt}(\sigma^*(t)-\sigma^*(o)) = \sum_q \int_{-\infty}^{\infty} G\ (t)e^{i\omega_q t}[A^q,[A^{-q},\sigma^*(o)]] \qquad 23$$

or

$$\frac{d}{dt}[\sigma^*(t)-\sigma^*(o)] = \sum_q J^q(\omega_q)[A^q,[A^{-q},\sigma^*(o)]],$$

where the oscillating term in ω_q results from transforming the A^{*q} into the A^q operators.

If I and S belong to the same nuclear species, the problem simplifies greatly. Then, following the prescription for utilizing the density matrix to calculate a physical observable (Equation 11), one multiplies from the right by I_z to obtain the spin-lattice relaxation or by I_x to obtain the spin-spin relaxation. Using the standard spin commutation rules and computing the trace over the spin states, this procedure results in a form similar to the Bloch equations (Equation 8) for any one pair of spins

$$\frac{d\langle I_x^*\rangle}{dt} = -\frac{\langle I_x^*\rangle}{T_2} \quad .$$

Then one sums over all such spin pairs in the lattice, and this sum gives the ensemble relaxation rates below

$$T_1^{-1} = \frac{3}{2}\gamma_I^4\hbar^2\, I(I+1) \sum_{k\neq i}{}' \{J_{ik}^1(\omega_I) + J_{ik}^2(2\omega_I)\} \qquad 24$$

and

$$T_2^{-1} = \gamma_I^4\hbar^2\, I(I+1) \sum_{i\neq k} \{\frac{3}{8} J_{ik}^2(2\omega_I) + \frac{15}{4} J_{ik}^1(\omega_I) + \frac{3}{8} J_{ik}^o(o)\} \quad . \qquad 25$$

The quantum mechanical calculation confirms the elementary predictions of the classical model. In particular, it should be noted that T_1 relaxation has no zero frequency contributions from the spectral density function. The two spins must transfer energy to the lattice

at either $\hbar\omega_I$ or $2\hbar\omega_I$ for a change in the Zeeman energy and relaxation along the z-axis. These processes also contribute to any loss of phase coherence, i.e., to T_2. However, the primary loss of phase correlation comes from zero frequency terms which do not transfer energy from the spin system.

Each term of the relaxation equations can be explored by relating the q index to the interactions listed in equations 19 and described in Table 1. The q=o term involves the evaluation of local dipolar fields (I_zS_z) and a simultaneous spin flip of the form one up-one down (I^+S^-). For like spins, these conserve the spin system's energy but destroy the phase coherence giving a T_2 relaxation. The strength of the local dipolar fields can give structural or positional information about the spins. The remaining terms depend upon some lattice action to excite the spin system and cause a quantum level population change. It is possible to change by one quantum of energy (I^+S_z-like terms) or two (I^+S^+-like terms). If the motions have spectral components at these frequencies, translational jumping, rotational motion, or molecular vibrations could cause the lattice to affect the energy transferring terms.

In many systems an additional complication arises from the presence of unlike spins. By following the same theoretical prescription and allowing for the different nature of the S spins, the I spins in the presence of both I and S spins will relax at the rates

Table 1. Motional contributions to I spin relaxation rates

SPIN and LATTICE ACTION	I SPIN ENERGY CHANGE	LATTICE JUMP FREQUENCY	CONTRIBUTES TO RELAXATION RATES:	SPIN OPERATORS
I spin precesses in local fields from I'_z, S_z	none	zero	T_2	$I_z I_z'$, $I_z S_z$
Spin flip-flop between two I spins	none	zero	T_2	$I^+ I'^-$, $I^- I'^+$
I spin jumps past either I' or S spin; I spin flips	$\hbar\omega_I$	$\nu=\omega_I$	T_2, T_1	$I^\pm S_z$, $I^\pm I_z'$
I spin jumps past S spin; both flip	$\hbar\omega_I$	$\nu=\omega_I \pm \omega_S$	T_2, T_1	$I^+ S^-$, $I^- S^+$
I spin jumps past I' spin both flip	$2\hbar\omega_I$	$\nu=2\omega_I$	T_2, T_1	$I^+ I'^-$, $I^- I'^+$

$$T_1^{-1} = \frac{2}{3} M_{II}\gamma_I^2\{F(\omega_I) + 4F(2\omega_I)\}$$

$$+ \gamma_I^2 M_{IS}\{\tfrac{1}{2}F(\omega_I - \omega_S) + \tfrac{3}{2}F(\omega_I) + 3F(\omega_I + \omega_S) \qquad 26$$

and

$$T_2^{-1} = \gamma_I^2 M_{II}\{F(o) + \tfrac{5}{3}F(\omega_I) + \tfrac{2}{3}F(2\omega_I)\}$$

$$+ \tfrac{3}{2}\gamma_I^2 M_{IS}\{\tfrac{2}{3}F(o) + \tfrac{1}{6}F(\omega_I - \omega_S) + \tfrac{1}{2}F(\omega_I) + F(\omega_S) + F(\omega_I + \omega_S)\}$$

27

where M_{IS} and M_{II} are the squared mean field strength at the I site from the S spins and other I spins, respectively. The frequency ω_S is the precession rate of the S spins. $F(\omega)$ is the functional form of the spectral density function after the various constants have been evaluated as coefficients or absorbed into M_{II} or M_{IS}.

These equations pertain only when the S system's spin-lattice relaxation is much, much faster than that of the I system so that saturation of the S system cannot occur. If this situation does occur, the relaxation rates are described by still further terms reflecting these saturation effects.

If diffusional motion is the cause of the local field fluctuations exciting transitions between the energy levels, the model developed in the section covering diffusion (Chapter III) gives the appropriate relaxation rates. This model is most useful in the case of isotropic jumping motion and uncorrelated spin motions as found in powder or liquid samples. The correlation function is fourier transformed into a Lorentzian function $F(\omega)$,

$$F(\omega) = \tau_c(1 + \omega^2\tau_c^2)^{-1}, \qquad 28$$

where τ_c is the correlation time in this model. Because both hydrogens can jump and the tantalum atoms do not, the correlation time for the hydrogen-hydrogen jump is just one-half of the hydrogen jump time from the neighborhood of a tantalum site.

Figure 5 shows the predicted behavior of the relaxation rates when the correlation time has an Arhennius dependence on temperature. The prominent characteristics are, first, a minimum in T_1 when $\tau_c \approx \omega_o^{-1}$; second, on either side of the minimum value the slope of $\ell n\ T_1$ vs. inverse temperature (therefore, also vs. $\ell n\ \tau_c$) is proportional to the activation energy; and third, the steady decrease of T_2 to a limiting value. The limiting value is defined by the local field strength in the long correlation time limit.

In addition to the dipolar relaxation from other nuclear spins, the conduction electron spin interacts strongly with the nuclear spins in metals. The major portion of this mechanism comes from the Fermi contact interaction. The strength of the electronic contribution to the spin-lattice relaxation is proportional to the s-like character of the conduction band at the nuclear site. Originally derived by Korringa (27), this dependence is expressed as

$$T_1 T = C \langle |\psi_S|^2 \rangle_F \ , \qquad 29$$

where $\langle |\psi_S|^2 \rangle_F$ is the probability density of s-band electrons at the nuclear site.

These two different relaxation mechanisms may both be present and strong in the same sample. However, the characteristic minimum arising from diffusional motion clearly distinguishes between them.

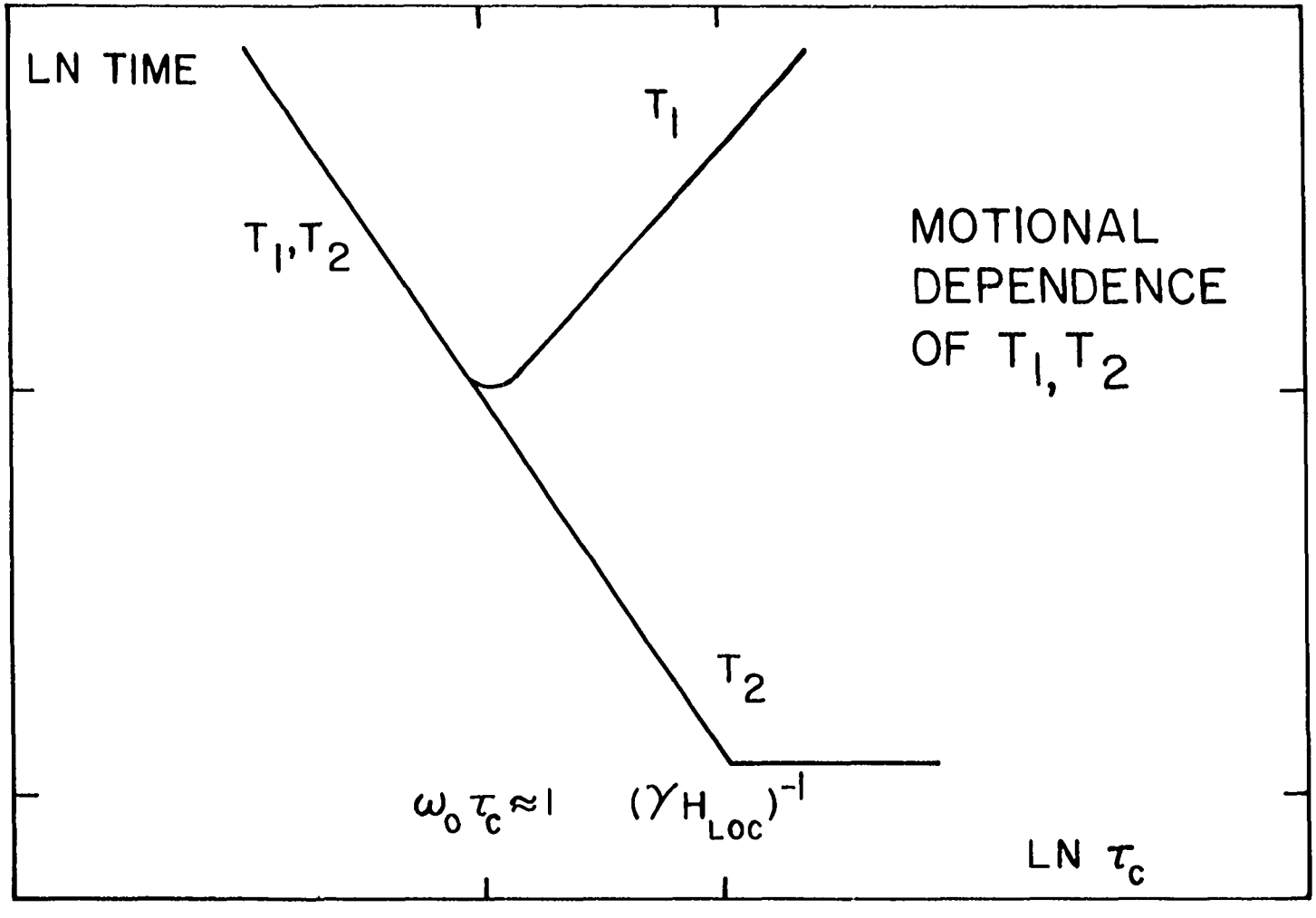

Figure 5. Atomic motions cause a definite pattern for the relaxation times as a function of the correlation time τ_c.

In summary, the temperature dependence of the two relaxation times yields several physical observables. First, a minimum in T_1 vs. T gives the correlation time or its inverse, the jump frequency, directly from the Larmor frequency. The actual value of the activation energy can be found from the slopes on either side of the minimum. Using the model in the diffusion section, the diffusion coefficient, D, may be estimated.

With an explicit form of the assumed spectral density function, the jump frequency may be plotted versus inverse temperature. This eliminates the curvature at the minimum and therefore increases the accuracy of the activation energy determination. The values of the minima of T_1 and T_2 relate to the structure through the quantities M_{II} and M_{IS}. Finally, the strength of the electronic contribution to the spin-lattice relaxation can be measured at temperatures well above or below the minimum and used primarily in a qualitative comparison with other hydride systems.

Additional models exist for the spectral density function of the diffusive motion; the most notable being that due to Torrey which takes into account the non-isotropic nature of the jumps and makes no assumption regarding the time correlation. Although it was applied successfully by Will (28), the Torrey theory has a difficult functional form and requires exact knowledge of the field strengths of the two spin species. M_{II} and M_{IS}, separately. The theory describes the shape of the minimum in T_1 well and gives a more complete description of the nature of the jump. A review of this theory can be found in Torrey (21) or Will (28).

Practical Considerations

Certain practical comments are useful to note at this point. First, when there are two processes acting simultaneously in a single homogeneous sample, the resulting relaxation rates add to produce only a single spin-lattice decay. By contrast, when two separate physical domains in a sample have differing relaxations, the recovery curve reflects the relative amount of each domain present and hence of the two relaxation rates. However this statement is ambiguous for T_2; there may be structural differences from site-to-site within a homogeneous sample, resulting in different rates of de-phasing for different sites. Since the spins are all mutually interactive (by the statement of homogenity), the processes transferring energy to the lattice are the same for all spins. An equivalent approach is that while a spread in the local field will drastically affect the sums of the dipolar pairs in the T_2 process, such a spread amounts to only a very small variation when compared to the applied field value, which determines the resonant frequency and hence the most effective jump frequency, and is therefore negligible.

The theory of diffusional dipolar relaxation has been successfully applied to many problems in liquids and solids. Among these may be noted self-diffusion in lithium and sodium metals (29) and hydrogen diffusion in a wide variety of hydrides (30).

CHAPTER V. EXPERIMENTAL METHOD

Pulsed NMR

Most of the measurements for this thesis were made with a pulsed NMR spectrometer described in the Equipment Chapter. The response of the magnetization to sequences of pulses traces the recovery of the magnetization to equilibrium. For clarity, the effect of the pulses is given here using a semi-classical model. More thorough semi-classical treatments are to be found in Farrar and Becker (24) and in Slichter (25) and a thorough quantum treatment in Mehring (31).

The creation of a non-equilibrium magnetization and the observation of its recovery are accomplished by a sequence of one or more short pulses of the resonant radio frequency radiation. Figure 6 illustrates the following discussion in both the lab and the rotating frames. The radio frequency coil is positioned so that its axis is perpendicular to the applied field. This coil contains the sample which is irradiated by the oscillating magnetic field caused by each rf pulse. Although this field oscillates parallel to the axis of the coil, it can be divided into two superposed counter-rotating fields, each having one-half the intensity of the oscillating one. One of the rotating fields has the appropriate direction to fulfill the resonance condition (Equation 6) if the pulse is applied at the Larmor frequency. The other has little effect since its direction of rotation places it $2\omega_o$ away from the resonant condition. Furthermore, by choosing the phase of the rf current applied to the coil, the relative direction of the magnetic field pulse

Figure 6. A radio frequency coil whose axis is perpendicular to the strong static magnetic field produces an oscillating magnetic field when driven by a high frequency alternating current. In a coordinate frame rotating at the oscillation frequency one component appears static and its direction depends upon the phase angle of the driving current.

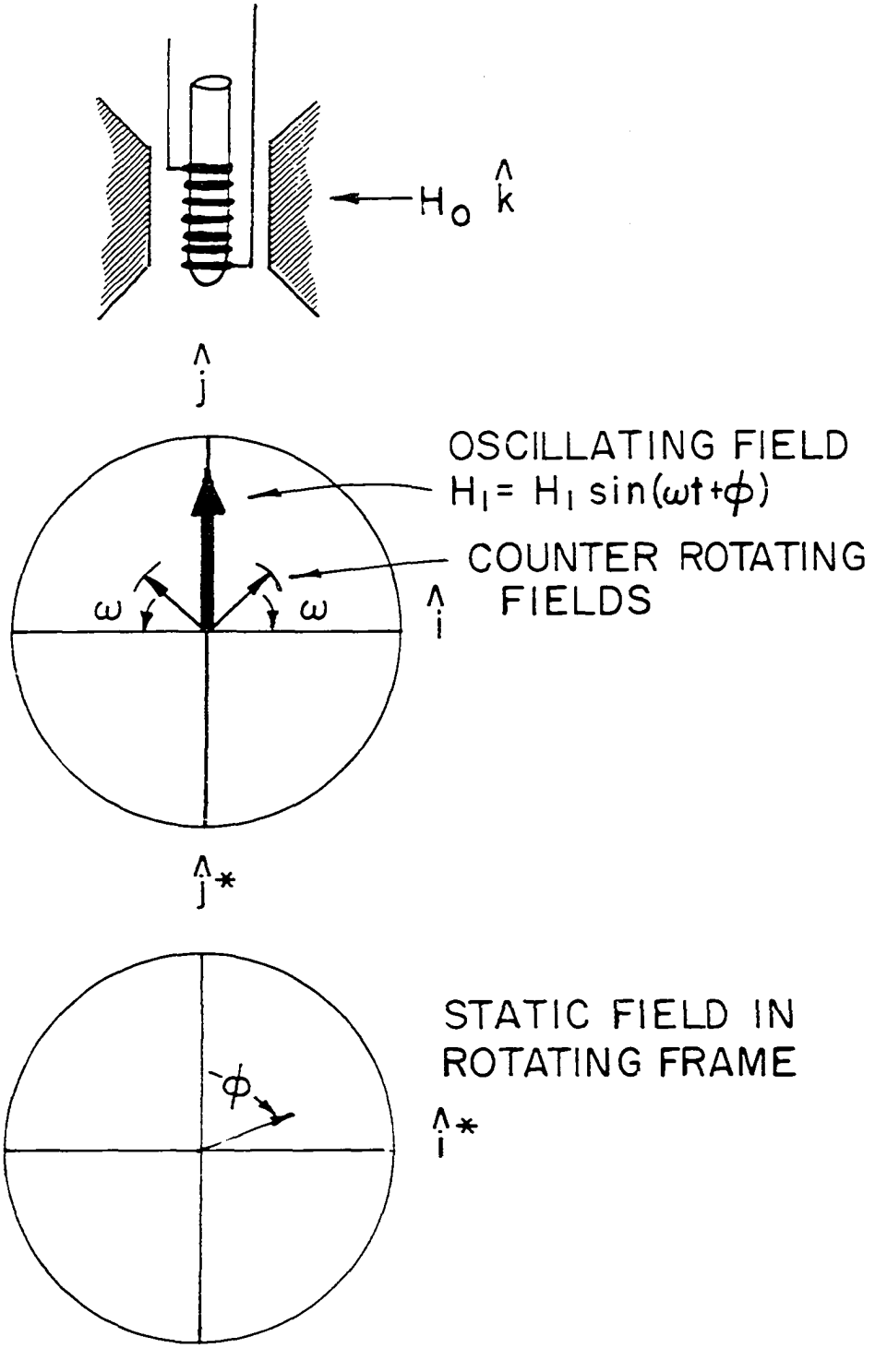
$H_o \hat{k}$
$\hat{j}$
OSCILLATING FIELD
$H_1 = H_1 \sin(\omega t + \phi)$
COUNTER ROTATING FIELDS
ω
ω
$\hat{i}$
$\hat{j}^*$
$-\phi$
STATIC FIELD IN ROTATING FRAME
$\hat{i}^*$

in the rotating frame can be varied. In much the same manner, the in-phase and quadrature signal components in the xy rotating plane can be detected separately by varying the reference phase to the phase sensitive detector.

In the rotating frame, the field developed by the radio frequency current is stationary. Then the torque equation in the rotating frame will be,

$$\frac{d\vec{M}}{dt} = \gamma\vec{M} \times \vec{h}_{rf}$$

If the $\vec{h}_{rf}$ is chosen to be in the $\vec{j}^{*}$ direction and momentarily all other fields are ignored, the solutions are

$$M_z = M_o \cos \gamma h_{rf} t$$

$$M_x = M_o \sin \gamma h_{rf} t \ ,$$

assuming that $\vec{M}$ was originally along the z-axis. A necessary condition for this to hold is that the applied rf field be greater than the local interaction fields. If the pulse is left on for a time t, the magnetization is turned through an angle

$$\theta = \gamma h_{rf} t \qquad 30$$

Thus a short pulse of radio frequency magnetic field can produce non-equilibrium situations, changing the spin system energy or producing coherently phased spins.

In particular, the magnetization can be forced into the xy plane with a $\theta = 90^{o}$ pulse, and the decay of the magnetization will be observed as decreasing intensity of the resonance frequency signal. The distribu-

tion of internal local fields is primarily responsible for this decay. Since some nuclei have slightly higher resonance fields due to the distribution of local field values, the contributions that these nuclei make to the total magnetization precess away from the x-axis in the rotating frame and thus result in a dephasing process. The recovery to random phasing in the xy plane is called a free induction decay (fid), and is shown in Figure 7. A difference ΔH between the applied field value and the resonance field (corresponding to the rf of the pulsed field) appears as additional precession in a coherent manner in the rotating frame causing a beat frequency to be superimposed on the signal. This beat frequency is just $\gamma \Delta H$.

The time constant of the decay following a 90° pulse by definition should be T_2, the spin-spin relaxation time. However, the inhomogenity of the applied magnetic field is often of the order of or greater than the distribution of local fields resulting from the dipolar interaction with other nuclear dipoles. Then, the inhomogenity masks the real decay. To avoid this problem, the spin-echo techniques are used. Originally conceived by E. L. Hahn (32), the application of a 180° pulse after a time τ causes a re-focussing of the moments at time 2τ to form an echo. The 180° pulse rotates the moments about the h_1 axis as shown in Figure 7. The mechanisms causing the moments to dephase retain their spatial distribution so that the fastest moments have the greatest angle through which to precess and the slowest, the smallest. As illustrated in Figure 7, the simultaneous rephasing of all these

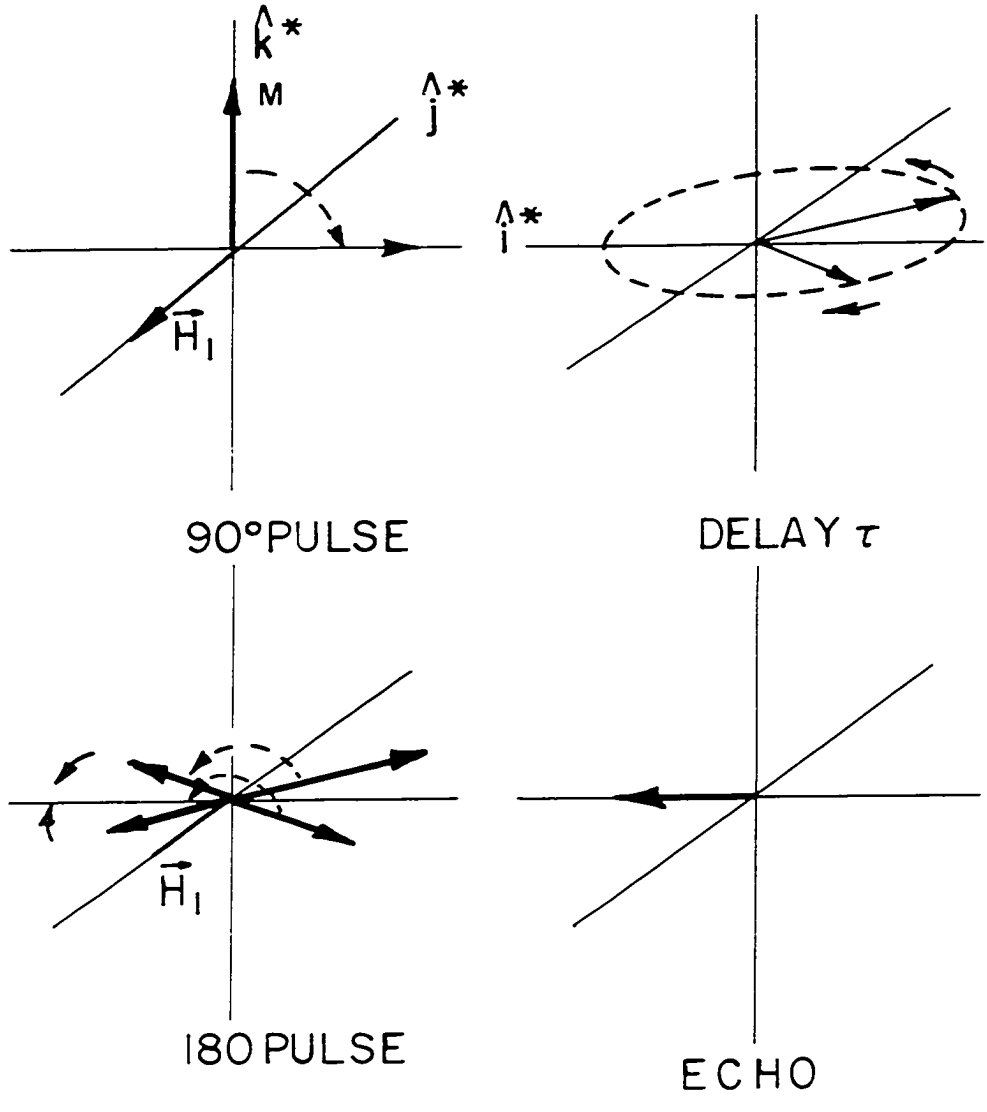

Figure 7. A 90° pulse rotates the magnetization into the x-y plane in the rotating frame, where it can induce a voltage in the radio frequency coil. Local fields then cause a precession from this axis and a decrease in the measured signal. After a time τ, a 180° pulse rotates the magnetization about the axis. Since the physical environment of each moment is unchanged, each moment continues to precess in the same direction, causing an echo when the components rephase at time τ after the 180° pulse. The amplitude of the echo varies as $\exp\{-2\tau/T_2\}$.

moments causes an "echo". The amplitude of the echo decreases with increasing separation in time but its rate is now the true T_2.

For convenience of measurement and elimination of systematic errors, the Carr-Purcell (CP) sequence (33) and the Meiboom-Gill modification (34) to the CP sequence (CPMG) are usually the measurement techniques used. Although the refocusing 180° pulse creates an echo, it does not fundamentally change the recovery of the spin system, and it leaves the magnetization in the xy plane. Another 180° pulse would again produce a refocusing effect. If, then, successive 180° pulses are spaced at 2τ, the echoes occur at time τ after each pulse and describe the relaxation exactly. The echoes alternate in sign but their absolute magnitudes yield the relaxation rate in a single sequence. This amounts to an incredible saving in experimental time.

The disadvantage of this method is that any error in the 180° pulse length accumulates throughout the sequence. The modification proposed by Meiboom and Gill alleviates this difficulty by shifting the phase of the 180° pulse 90° with respect to the first 90° pulse and to the detector reference phase. All the echoes now refocus on one axis, and the errors in pulse length do not add as much error to the measurement. For a more thorough discussion see Meiboom and Gill (34) and Vold et al. (35).

A different sequence measures the spin-lattice relaxation time T_1. The most accurate and commonly used is the 180°, τ, 90°. The initial 180° pulse inverts the populations of the spin levels and raises the

spin system's energy. Because only magnetization components in the xy plane induce a voltage in the coil, no signal appears. As the magnetization recovers, it is described by

$$M_z = M_o(1 - 2\exp(-t/T_1)) \quad . \qquad 31$$

When a 90^o pulse is applied after a delay, the relative amplitude of the free induction decay is proportional to $M_z(t)$. Varying the spacing between the two pulses allows the experimenter to measure T_1, as shown in Figure 8.

Experimental Criteria

The consistency of the results of the experiments depend upon accurate adjustment of the pulsed NMR equipment and setting the measurement parameters to eliminate systematic errors. Adjustments of the electronics are covered in the equipment section. However, special attention needs to be paid to the setting of the measurement parameters such as pulse spacing and sequence repetition rate.

The most crucial difficulty for the extraction of the time constants from the recovery data is the determination of the equilibrium (steady-state) magnetization. This is used as a zero for the logarithmic plots and may systematically alter the derived time constant if not carefully determined. After five time constants from the start of the sequence, the changes in the magnetization should be less than one percent of the final value. For most of the experiments, the final signal values judged to be the equilibrium values occurred six or more decay constants after the start of the sequence. In the case of the free

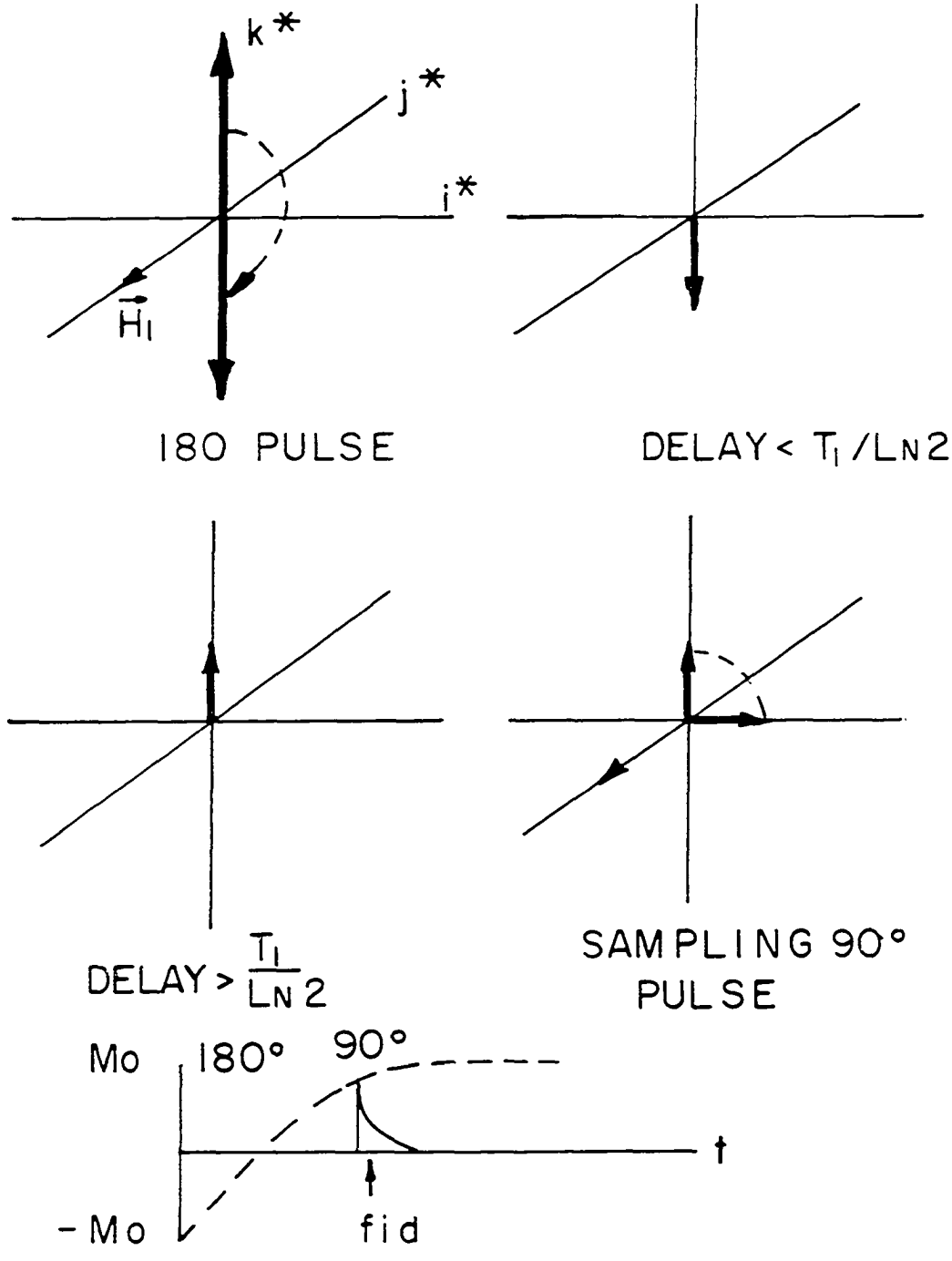

Figure 8. The 180°, -, 90° pulse sequence measures T_1 by inverting the magnetization and then sampling the z component at various time intervals with 90° pulses. The magnitude of the free induction decay (fid) is proportional to the z component of the magnetization.

induction decay measurements, this requires adjusting the length of the sweep time until the amplitude versus time data becomes a constant at long times. When the automated CPMG sequence is used, the number of echoes is extended to meet this same criterion.

Spin lattice relaxation times require an evaluation of M_o in order to extract T_1 from equation 31. Since this signal is not close to zero voltage, as in the previous cases, the value found may have larger statistical errors than in the other measurements. Therefore, the usual approach was to sample the free induction decay for many points in the interval between five and six T_1's and average the values to determine M_o.

A closely related problem involves determining a spacing between sample points in the CPMG and 180, τ, 90 sequences. For the CPMG technique, the major constraint is to avoid placing pulses inside the echoes. The 180, τ, 90 sequence must involve enough samples at long times to achieve a good average equilibrium magnetization, as discussed in the preceding paragraph. This is usually the best criterion for choosing the pulse spacing. In both cases, it is more effective to record smaller numbers of data points with larger spacings to avoid small system drifts which may affect the results.

Each of these sequences depends upon the spin system being in equilibrium at the time of the initial pulse. Therefore, the period between entire pulse sequences must be five or more spin-lattice relaxation times. If this criterion is not met, the pulse sequence

may combine the two relaxation rates, diminish in intensity, or add systematic error to the baseline evaluation.

Data Reduction

For the spin-lattice and CPMG sequences, data reduction was accomplished by a least-squares fit to a statistically weighted exponential. Statistical weighting is correct in these experiments because the digitizing process involves an events counter for which the uncertainity is the square root of the number of the counts.

The PDP-15 computer (Digital Equipment Corporation) usually handled this task through an interface to the digitizer. With the ability to read and write data to the Nicolet digitizer, the computer analyzed the data, printed out the fit parameters, and wrote the fit and the data logarithmically into the Nicolet memory. This instrument has a display overlap capability so that the data and the fit could be compared visually on an oscilloscope screen.

The fits were occasionally cross-checked by hand plotting the data on logarithmic paper. The agreement was always quite good. In addition, free induction decay measurements, and very fast spin-spin echo experiments were also reduced by hand. The free induction decays were not always exponential and the fast echo processes could not be collected automatically due to equipment limitations.

Under certain conditions discussed in the Nuclear Magnetic Relaxation chapter, non-exponential recovery was observed. Physically, this was expected to be the sum of two exponentials. Determining the

parameters of either or both decays is made difficult by the similarities of the two decay times and amplitudes. Several attempts were made using complex schemes of data analysis from Bevington (36) as well as simple schemes using a fit to the longer times and extraction of the short relaxation time. Although the fits improved from a single exponential, no consistent results were obtainable.

The Nicolet-PDP-15 combination did prove valuable for the problem of the two exponential decays. When the fit versus data was displayed on the oscilloscope, the onset of these regions could be detected and the relative amplitudes estimated.

Temperature Criteria

Because temperature is the independent variable in the overall analysis of the relaxation time behavior in these hydrides, it must be carefully controlled and measured. In addition, care must be taken to insure the sample has achieved thermal equilibrium and to avoid supercooling effects. Some difficulties have been reported for hydride systems (37) from these effects. A waiting time of one-half an hour or longer is typically appropriate for thermal equilibrium. However, supercooling is avoided by always heating the sample from lower temperatures when changing temperatures. Superheating is a much smaller effect and thus heating is the proper direction for temperature changes when phase transitions are present.

CHAPTER VI. EXPERIMENTAL EQUIPMENT

The experimental program made diverse demands for equipment functions. In some instances, the demands made upon the spectrometer system were contradictory so that design compromises had to be made. Equipment will be discussed in a roughly functional order, and such an order may occasionally be artificial. Figure 9 will aid the electronics discussion in its interconnections of various logical subsystems.

Magnet

The strong laboratory field (H_o = 9.3950 kOe for a resonant frequency of 40.000 MHz) was produced by a Harvey-Wells 12" electromagnet. During the course of the experiment, both the 1 3/4" and the 3" gaps were used. In both cases the magnet was stable within our detection limits for days, although the resonances were checked closely throughout any measurement period. The static field gradient (dH_o/dZ) was measured by a free induction decay experiment (see Chapter V) on a sample of glycerol which has a very long T_2. The result was a gradient of 0.4 Oe/cm.

Programmer

The major control for the experiment is the pulse programmer. It furnishes the switching network to the transmitter with the logical pulses to produce the radio frequency pulses and also triggers to display and record recording devices. The programmer is derived from a

Figure 9. The pulsed NMR spectrometer consists of digital, radio frequency, and audio frequency circuits. The sample is contained in the coil at the far right. The small blank boxes are the series diode arrangements for separating the transmitter pulses from the NMR signals. The light interconnecting lines indicate switching and trigger digital pulse connections, the intermediate intensity lines indicate the radio frequency pulse and signal connections, and the heaviest lines the detected audio signal paths.

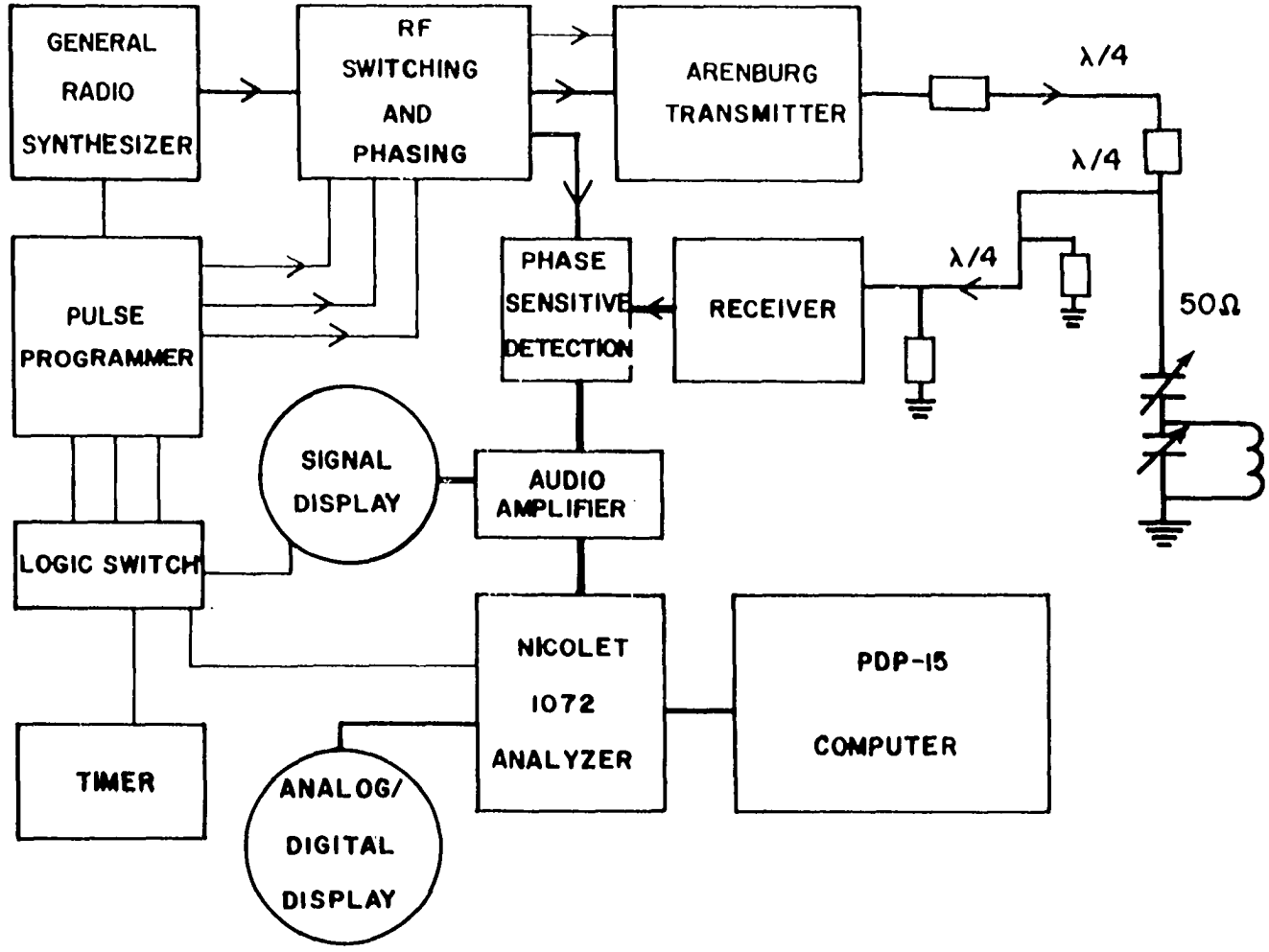
GENERAL RADIO SYNTHESIZER
RF SWITCHING AND PHASING
ARENBURG TRANSMITTER
λ/4
λ/4
λ/4
50Ω
PULSE PROGRAMMER
PHASE SENSITIVE DETECTION
RECEIVER
SIGNAL DISPLAY
AUDIO AMPLIFIER
LOGIC SWITCH
NICOLET 1072 ANALYZER
PDP-15 COMPUTER
TIMER
ANALOG/ DIGITAL DISPLAY

design by Conway and Cotts (38). In addition, an auto-increment module was added to facilitate spin lattice relaxation measurements by stepwise delaying the second pulse so that the measurement could be done in a hands-off manner (39).

To provide a brief outline of programmer function, the substance of the logic and switching arrangements are briefly discussed. First, a clock module establishes the repetition rate of the pulse sequence. When a start signal goes out from the clock, the first of several possible channels produces an output logic pulse. The output pulses from any one channel module are fixed to one variable duration and phase. Timing pulses for the next channel starts and the triggers are independently selectable as well. With two such channel modules one can create the previously described pulse sequences.

The output pulses from the programmer determine the duration of the radio frequency (rf) pulses through the rf switching module. There are two separately selectable paths activated by the pulses which are variable in phase and amplitude. Since relative phase changes in the rf change the field direction in the rotating frame, this feature allows the Meiboom-Gill experiment and the 90° phase shift detection of the on-resonance condition. The transmitter is further isolated by an "or" of the two paths after they are electronically summed. The switching module also contains the capability of varying the reference phase to the phase sensitive detector.

Transmitter Chain

The radio frequency source used for this experiment is a General Radio 1061 synthesizer which produced low phase noise rf oscillations at a frequency of 40.000 MHz and provided a coherent time base for the programmer with its external reference signal.

The combination of a continuous phase-coherent source and a time base which is definitely related to the phase of the rf pulse is therefore created. These are important criteria for the stability of multiple pulse measurements and phase sensitive detection.

The rf pulse is then amplified to approximately 800 watts of power by an Arenburg Ultrasonics PG-650C power amplifier. This transmitter produces a strong enough rf pulse to meet the rotating frame condition of $H_{rf} > H_{loc}$ in the sample.

The Probe System

The probe system has several functions and is designed along the lines of Lowe and Tarr (40) and Gottlieb et al. (41). Although the system must deliver high power rf pulses to the sample coil, it must also allow detection of a very low power signal induced by the nuclear moments approximately a microsecond after the pulse. The arrangement of cables, diodes, and the matching device is used to achieve this compromise.

Use of pairs of diodes connected in parallel but with opposite polarity is the major feature of the system. Such pairs conduct for high voltages but do not conduct for voltages less than one volt. The

first two sets of diodes serve only to prevent reflections from returning to the transmitter and eliminate noise to the receiver from such reflections. At the junction, the high voltage pulse may proceed in two directions. In the branch which has the one-quarter wavelength cable and the diode set connected to ground, the high voltage sees a high impedance resonant circuit which dissipates no energy. The other path contains the matching system tuned to the characteristic impedance at the operating frequency. This matches the load to the transmitter for the most efficient transfer of power to the sample coil.

Although the induced signal from the sample is blocked from the transmitter, it does travel directly to the receiver. As previously mentioned, the high voltage is shorted at the diode set after a quarter-wavelength. The only power dissipated is through the one volt offset needed for the diodes to conduct. The next quarter wavelength and diode set further reduce the high power rf pulse. The input to the receiver is then approximately one volt from the rf pulse and an unattenuated induced signal from the sample.

The matching system is shown in Figure 10. Containing the matching capacitors as independent mechanical units, the probe can withstand high voltages and operate in a cryogenic environment with external tunability. The temperature varying equipment attaches to the bottom along with the sample coil.

In order to avoid extraneous hydrogen nuclei in the vicinity of the sample, the sample coil was wound on a teflon form and the windings

Figure 10. Cross-sectional views of the concentric cylinder matching probe. Capacitors C_1 and C_2 are constructed of thin teflon separators between movable cylinders. C_1 is between the innermost brass cylinders at the bottom of the device, and the bolt at the bottom serves as the coil connection. The signal lead of the RG-58U cable passes through the top of the capacitor case as is shown in section BB. The ground lead is then connected to the case, and this becomes the second coil connection. The center lead of the cable connects to the second of the three brass cylinders and thus completes the circuit shown in the upper left corner. The capacitors are independently turnable in cryogenic environments and are capable of withstanding the high voltage rf pulses, without breakdown.

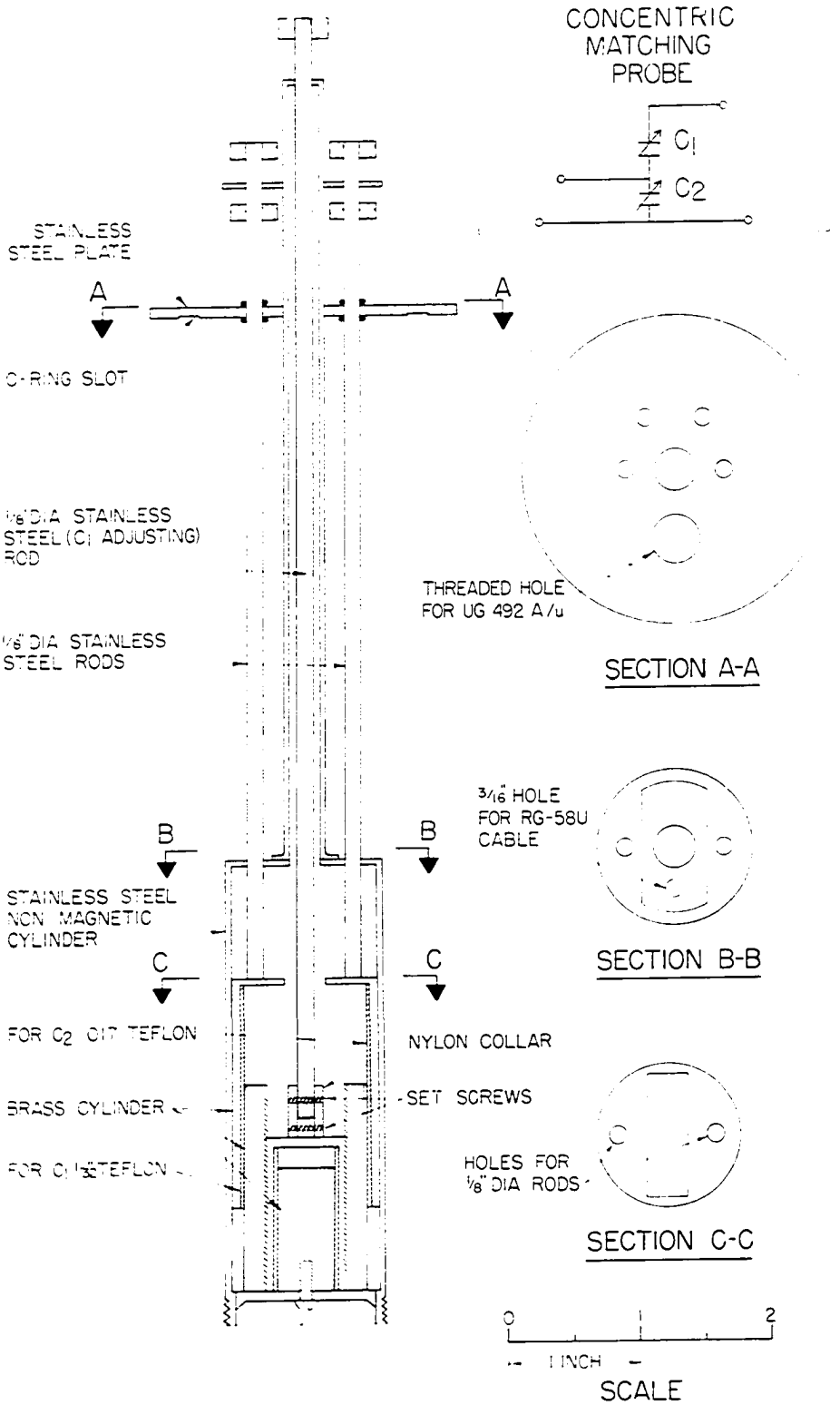
CONCENTRIC MATCHING PROBE
C1
C2
STAINLESS STEEL PLATE
A
A
O-RING SLOT
⅛" DIA STAINLESS STEEL (C1 ADJUSTING) ROD
⅛" DIA STAINLESS STEEL RODS
THREADED HOLE FOR UG 492 A/U
SECTION A-A
3/16" HOLE FOR RG-58U CABLE
B
B
STAINLESS STEEL NON MAGNETIC CYLINDER
C
C
FOR C2 CUT TEFLON
NYLON COLLAR
BRASS CYLINDER
SET SCREWS
FOR C1 TEFLON
HOLES FOR ⅛" DIA RODS
SECTION B-B
SECTION C-C
0
2
1 INCH
SCALE

were insulated with thin teflon tape. The coil was wound from a seven mil brass strap 3/16" wide to produce a large homogeneous rf magnetic field when pulsed. The use of brass eliminated the necessity of adding a resistor to reduce the Q of the coil. The low Q means that the system enclosing the probe disperses its energy quickly so that ringing continues in the coil for only a very short time.

The Signal System

The rf receiver consists of three Spectrum Microwave wideband limiting amplifiers (Model SML-D) with wideband tuned filters to eliminate parasitic oscillations (42). The amplification is approximately sixty decibels and is linear below an input level of 87 millivolts. The recovery time to full gain is less than one microsecond after an overload pulse.

The output of the receiver is phase-sensitively detected with respect to a variable phase source. The resulting video signal is the envelope of the rf compared to a reference phase. Variation of the reference phase corresponds to varying the axis of observation in the rotating frame. The video amplifier has variable gain to 55 db and a range of filter settings. The signal is then displayed on an oscilloscope and is input to the Nicolet 1072.

Data Storage

Depending upon the function and the time scale, three methods of data storage were used. For rapid free induction decays, a Biomation

610B offered the best short time resolution. For both CPMG and the 180°, τ, 90° sequences, the Nicolet was triggered in an external address advance mode, allowing the entire relaxation to be recorded. When the external advance trigger is received, the Nicolet stores the input information in memory and increments the storage address. In the CPMG case, the triggers for the external advance were set to coincide with the maxima of the echoes. In the auto-incremented 180°, τ, 90° sequence, the triggers advance the address and store data from a fixed point of the free induction decay into memory. Using other triggers to reset the channel address, both sequences can then be repeated to successively average over many complete recovery curves.

The stored data may be accessed directly from the Nicolet by digital readout, oscilloscope display or chart recorder. Alternatively, an interface built by the Ames Laboratory Instrumentation Group allows input and output from the Nicolet to a Digital Equipment Corporation PDP-15 computer for direct data reduction.

Electronics Adjustments

Although many adjustments are made on such a system, only the ones particular to the NMR equipment are covered here. These are meeting the resonance condition, determining the correct phase and duration of the pulses, and matching the transmitter to the coil for best power transfer.

The two independent mechanical capacitors are adjusted to create a match to the characteristic impedance at the operating frequency by

use of a Hewlett Packard 4815A Vector Impedance Meter. The coil should have approximately 0.4 microhenries inductance for the best match. The system is stable over a wide range of temperature and usually only needs to be retuned when coils or samples are changed.

The remaining adjustments must be made iteratively until no further improvement is seen. When a decay is visible after a pulse, the magnetic field, phase of the rf, and length of the pulse should be varied to achieve the strongest signal with a nearly exponential character. Since the null after a 180° pulse is more sensitive than the maximum of the decay, one uses the 180° pulse duration as a comparison for the necessary length of a 90° pulse. Typical 180° pulses were 2.5 microseconds long, corresponding to an applied rf magnetic field of 38 Oe. Using a spin echo sequence, the reference phase to the phase sensitive detector is varied to produce the most symmetric echo. This is then repeated by shifting the second pulse 90° in phase and adjusting that shift until the echo is symmetric but opposite in polarity to the previous case. Finally, the 90° pulse is shifted 90° as well, and the magnetic field is adjusted so that there is a null signal after the pulse. This set of adjustments is repeated until all of the parameters are at the best setting.

Temperature Systems

The experiment required a wide range of stable temperatures in the sample environment. Three separate systems were used to achieve the diversity needed. All three employed two copper-constantan

thermocouples for monitoring the sample environment and for feedback to the temperature controller.

The first method was immersion of the sample in liquid nitrogen and oxygen baths. The entire assembly was contained in a glass dewar.

The remaining two techniques both used the heater assembly of Figure 11. The sample is isolated in a copper cylinder with a heater wound on a bottom attachment. The assembly has a thin-wall stainless tube which then connects to the probe and contains the rf leads within it. Since thermal contact from the environment to the sample is by gas convection, the stainless steel tube is internally packed with glass wool to lower the convection gradient. At temperature extremes, the change in temperature across the sample was found to be only two degrees.

To achieve higher temperatures, the assembly was insulated and heated. Temperatures near 500 K were obtained with the system. Lower temperatures were reached by adding a heat leak of varying diameter and composition to the bottom of the heater assembly. A heavy copper block attached to the other end of the leak rod was immersed in liquid nitrogen, establishing a push-pull thermal system. The different leaks made operation over a range extending to 100 K possible. This system also proved very effective in improving stability near room temperatures with a slight cold leak to the sample.

Figure 11. The temperature control and variation for this experiment was accomplished by the heat leak arrangement shown here. The sample, coil, and the measuring thermocouple were placed in the copper cylinder in the lower left corner of the diagram. A heater was wound on the solid upper block below the sample with another thermocouple placed next to it for regulation. The entire assembly fastened to the bottom of the probe shown in Figure 10. For temperatures above room temperature only the portion shown was needed. When lower temperatures were deaired, a heat leak to liquid nitrogen temperature was made by attaching a rod with a large copper block at the lower end to the bottom of the sample assembly and then immersing the copper block in liquid nitrogen. Temperature variation was achieved by varying the heater current and the material or diameter of the leak rod. The entire leak system was enclosed in the stainless shell at the far right which provided mechanical stability. The gaps within the outer shell were packed with glass wool to reduce convection currents.

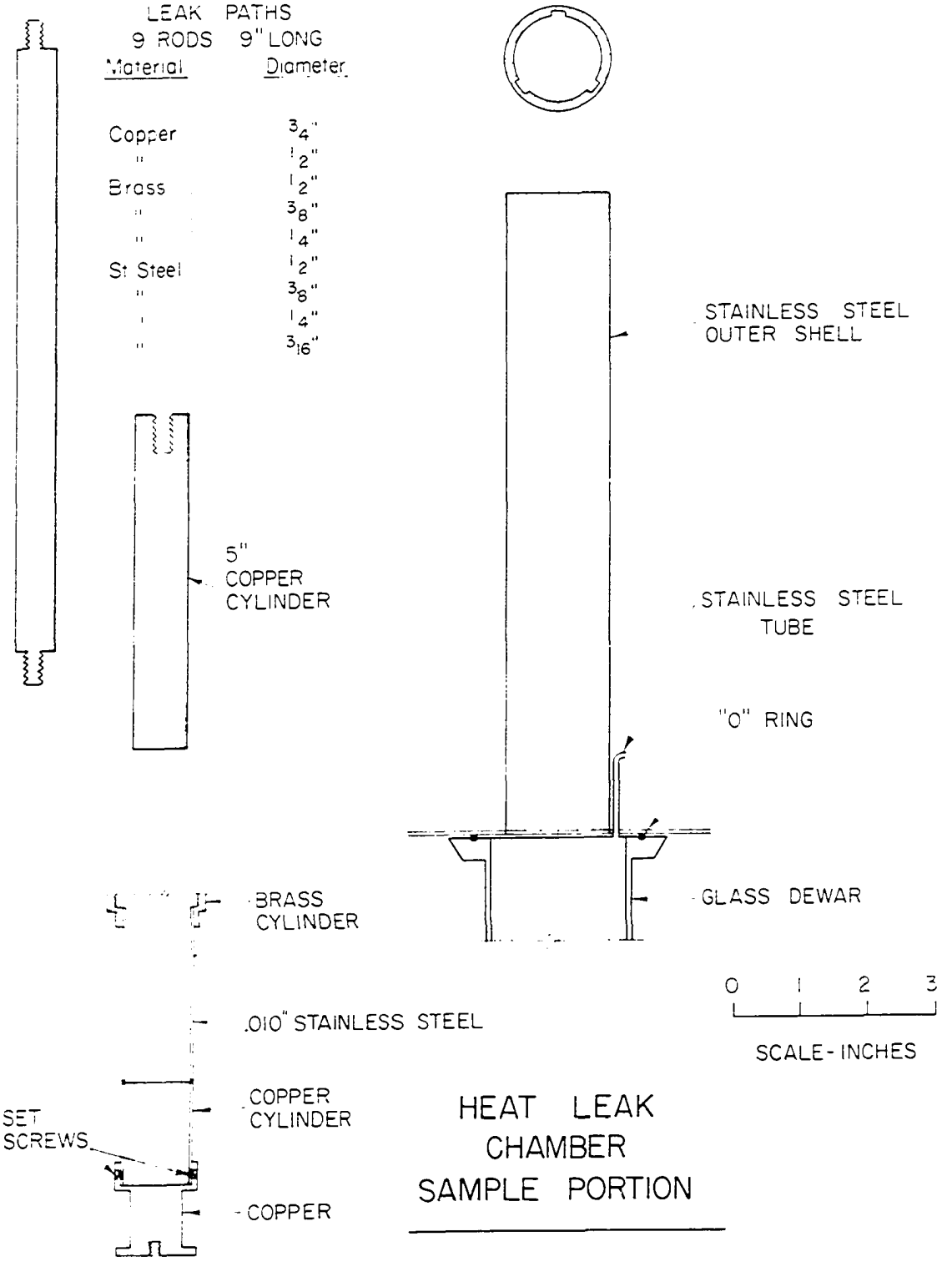

HEAT LEAK CHAMBER SAMPLE PORTION

CHAPTER VII. RESULTS AND DISCUSSION

The Vb hydrides have been the subject of much intense recent study by several groups. The structural, diffusive, and electronic nature of these hydrides still retain many unresolved features at this time. Figure 12 shows the best compilation of phase information for the tantalum-hydrogen system at the start of this study. Schober and Carl (8) (see Figure 1) have improved greatly upon this by using differential thermal analysis (DTA) on numerous single crystal samples. The great number of samples and the homogeneous single crystals contributed to the accuracy and completeness of their phase diagram. As a counter-example to Schober and Carl's work, Asano et al. (16) used powders of tantalum hydrides and report much less consistent results. As mentioned in Chapter II, certain regions of the phase diagram are not as well-understood as the Schober and Carl diagram would indicate, simply because DTA only shows when transitions occur, and not the structures involved.

Previous NMR investigations had provided a wide variety of information about these hydrides. Both Lutgemeier et al. (43) for niobium hydrides and Pedersen et al. (44) for tantalum hydrides showed that diffusion was the primary relaxation mechanism for proton spins over a wide temperature range about room temperature. Furthermore, these references indicated that a high temperature transition to the α phase appeared as a large (a factor of about 4) jump in the value of T_1. Pedersen et al. also noted some further effects in the tantalum-hydrogen system. First, composition and temperature regions exist in which recovery of the magnetization is characterized by a non-single exponential decay. These indications were

Figure 12. At the start of this study, a phase diagram was compiled from various sources.

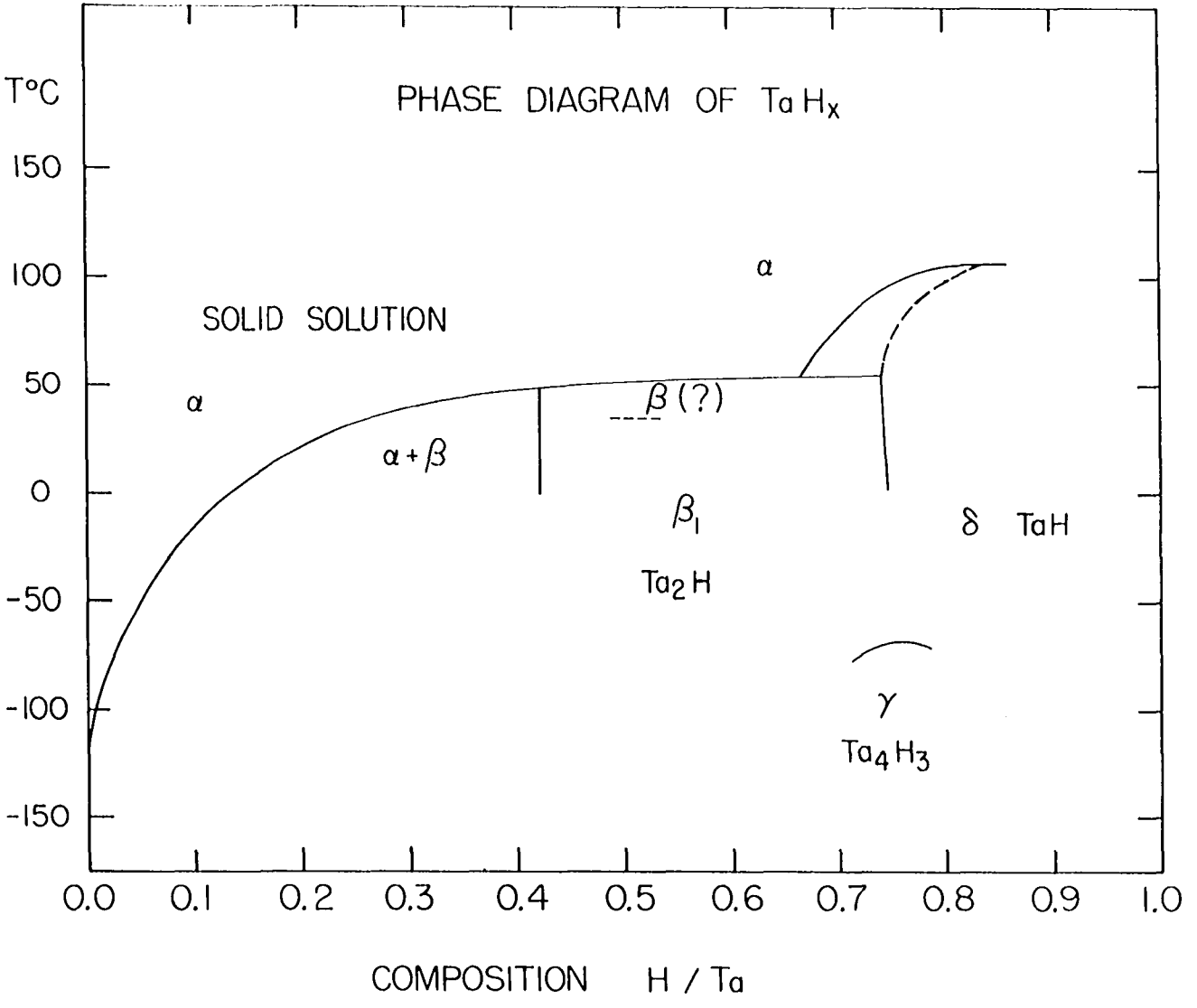
PHASE DIAGRAM OF Ta Hx
T°C
150
100
50
0
-50
-100
-150
SOLID SOLUTION
α
α
α + β
β (?)
β1
Ta2 H
δ TaH
γ
Ta4 H3
0.0
0.1
0.2
0.3
0.4
0.5
0.6
0.7
0.8
0.9
1.0
COMPOSITION H / Ta

not pursued further, however. As commented upon in the Experimental Methods chapter, the non-exponential decays were consistently difficult to parameterize, but were readily distinguished with the equipment. Second, Pedersen et al. noted discontinuities in the slope of T_1 versus 10^3T^{-1} and jumps in the value of T_1 corresponding qualitatively to the published structural data available at that time. The work done by Lutgemeier et al., and by Zamir and Cotts (45) showed similar relaxation characteristics for the niobium-hydrogen system. Lutgemeier et al. also extracted reliable information on the electronic contributions to the relaxation rates and diffusion energies. In addition, NMR investigations of the Knight shift (46) showed the bulk susceptibility causing a slight shift. And finally, an NMR study of vanadium hydride (47) reports motional processes dominate the spin-lattice relaxation rates.

The results of the present study are shown in Figures 13 through 18. The measurements presented are almost exclusively of spin-lattice relaxation times for reasons discussed later in this chapter. Much of the information presented here has features of the electronic, structural, and diffusive processes intermixed. In order to maintain coherence in this discussion, the α phase data will be analyzed first, the structural transitions seen in this study compared and listed next, and the complicated low temperature ordered phase diffusion processes will be modeled and discussed last.

The relaxation time plots for the six samples studied are placed in order of increasing hydrogen concentration. Only one plot (Figure 16) is graphed linearly with temperature to facilitate comparison with the

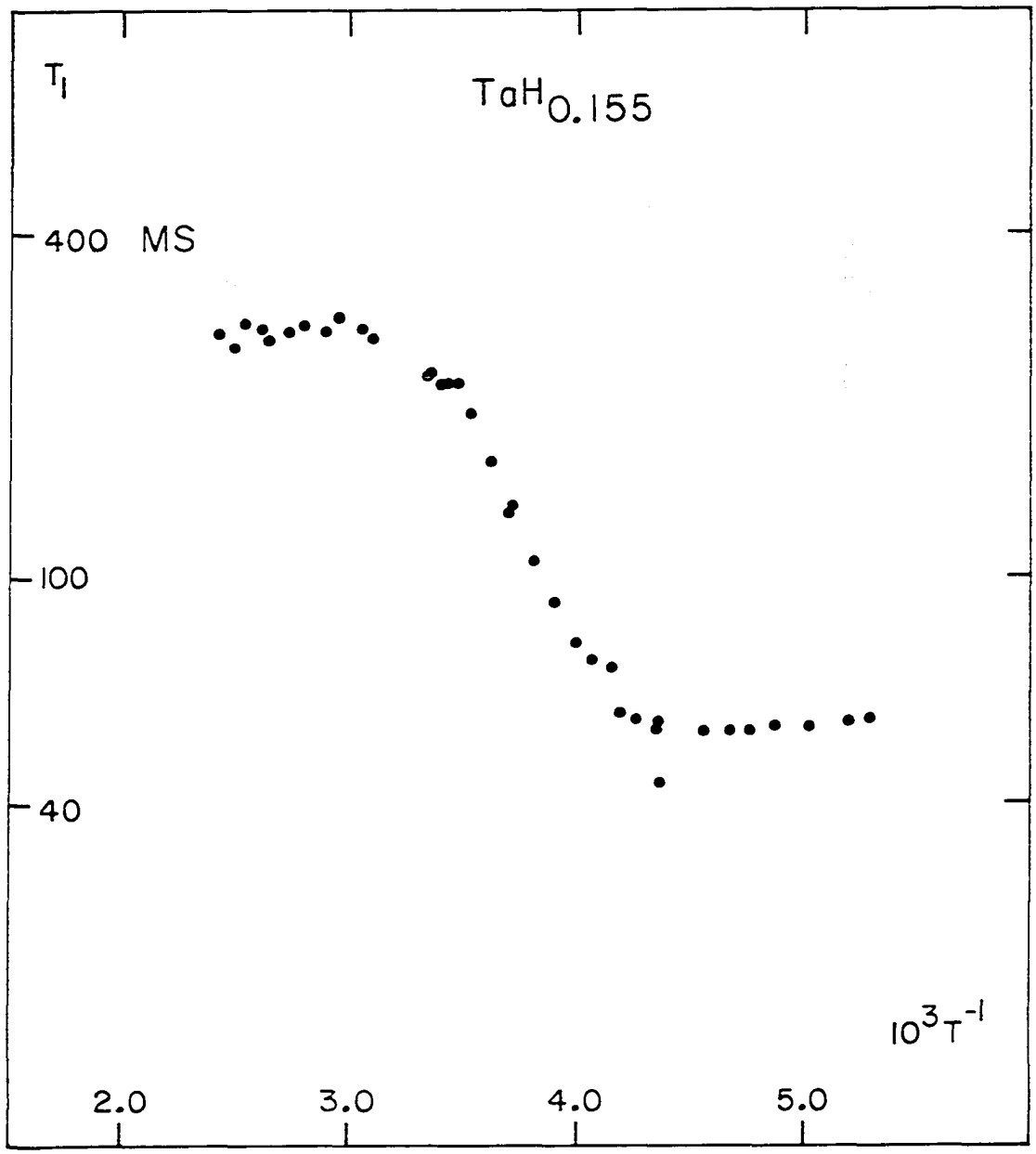

Figure 13. Proton spin-lattice relaxation times as a function of inverse temperature for the H/Ta = 0.155 sample.

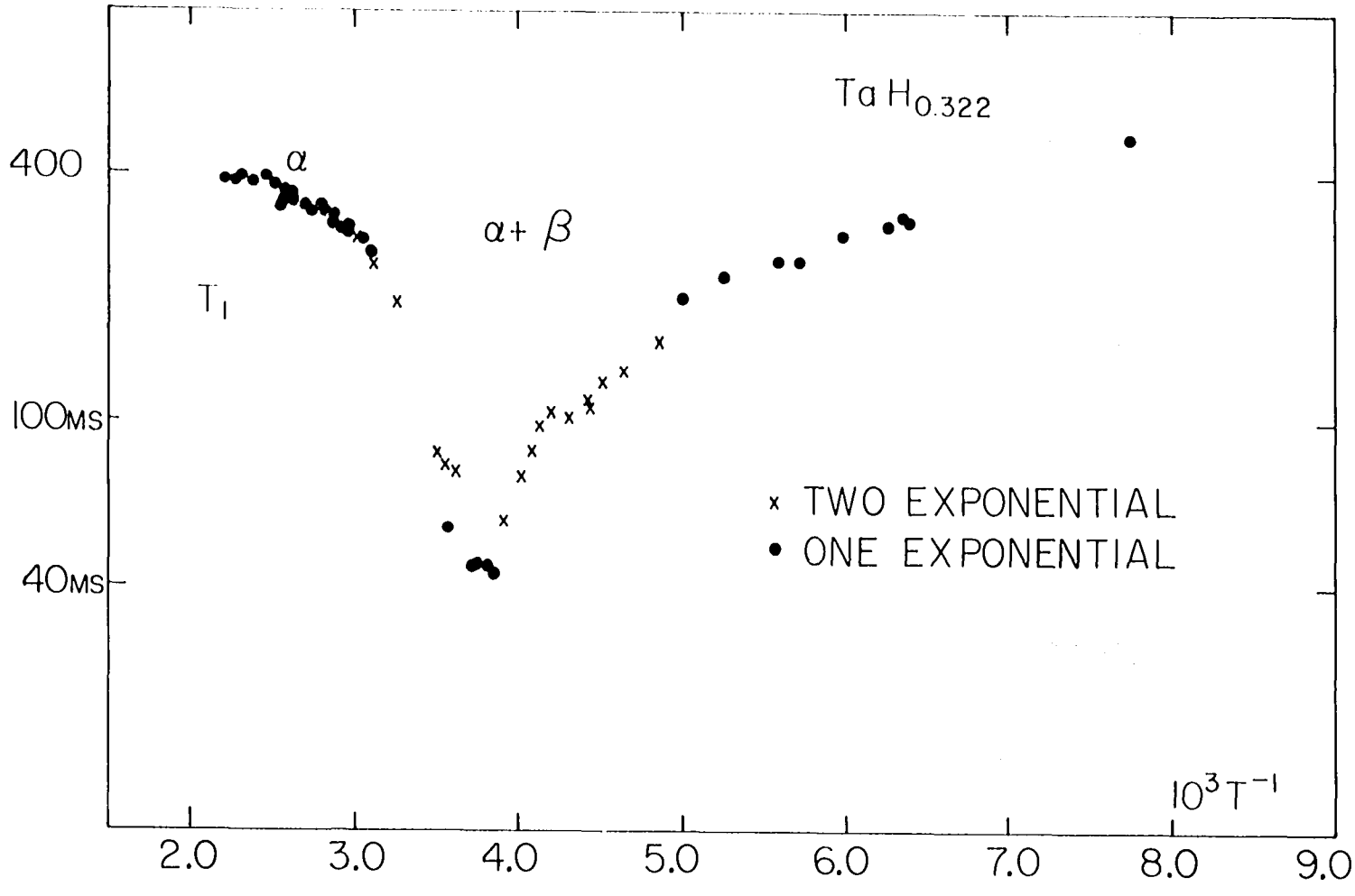

Figure 14. Proton spin-lattice relaxation time plot for the H/Ta = 0.322 sample shows the two phase region signature.

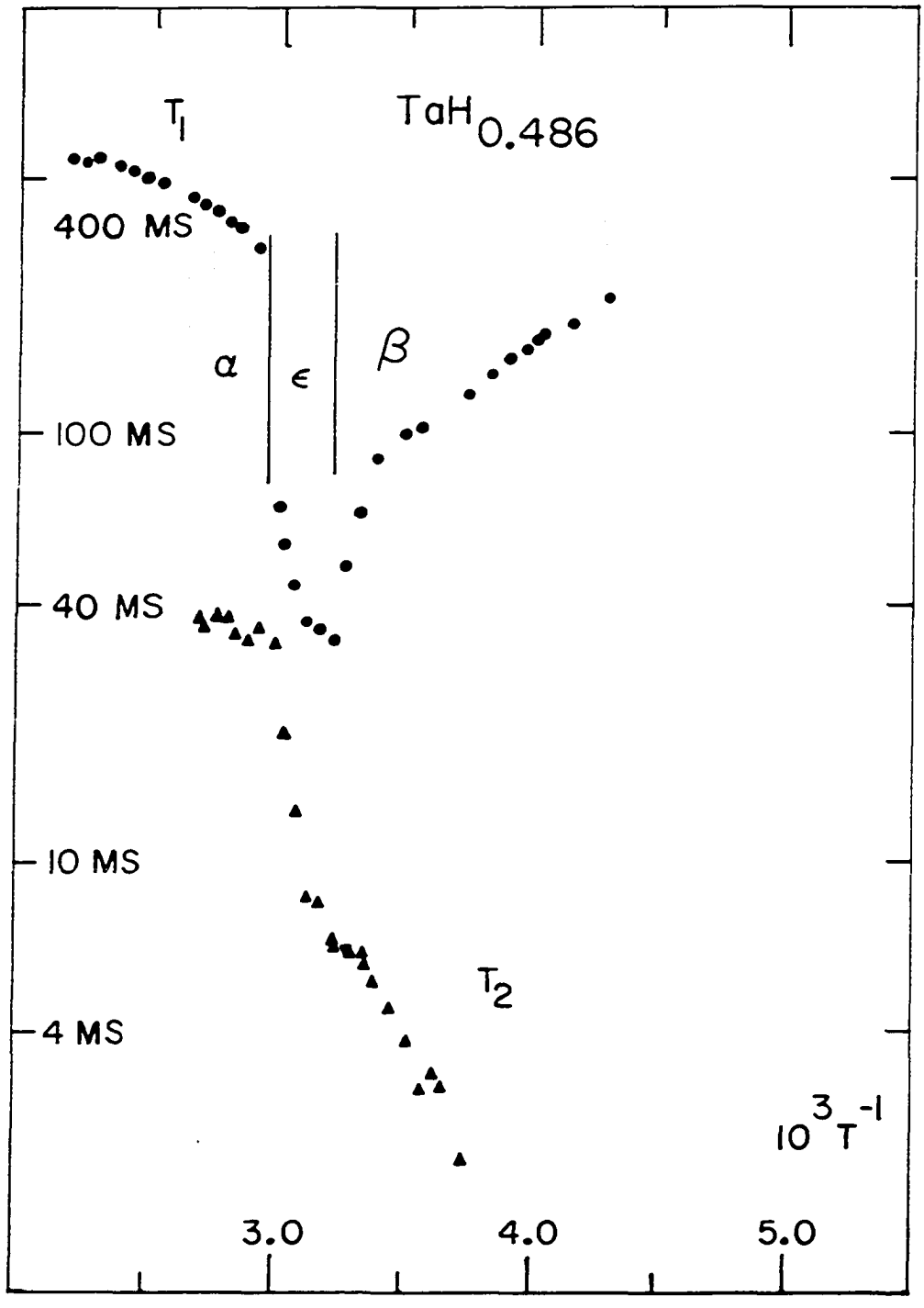

Figure 15. Proton spin-spin (T_2) and spin lattice (T_1) relaxation times for the H/Ta = 0.486 sample.

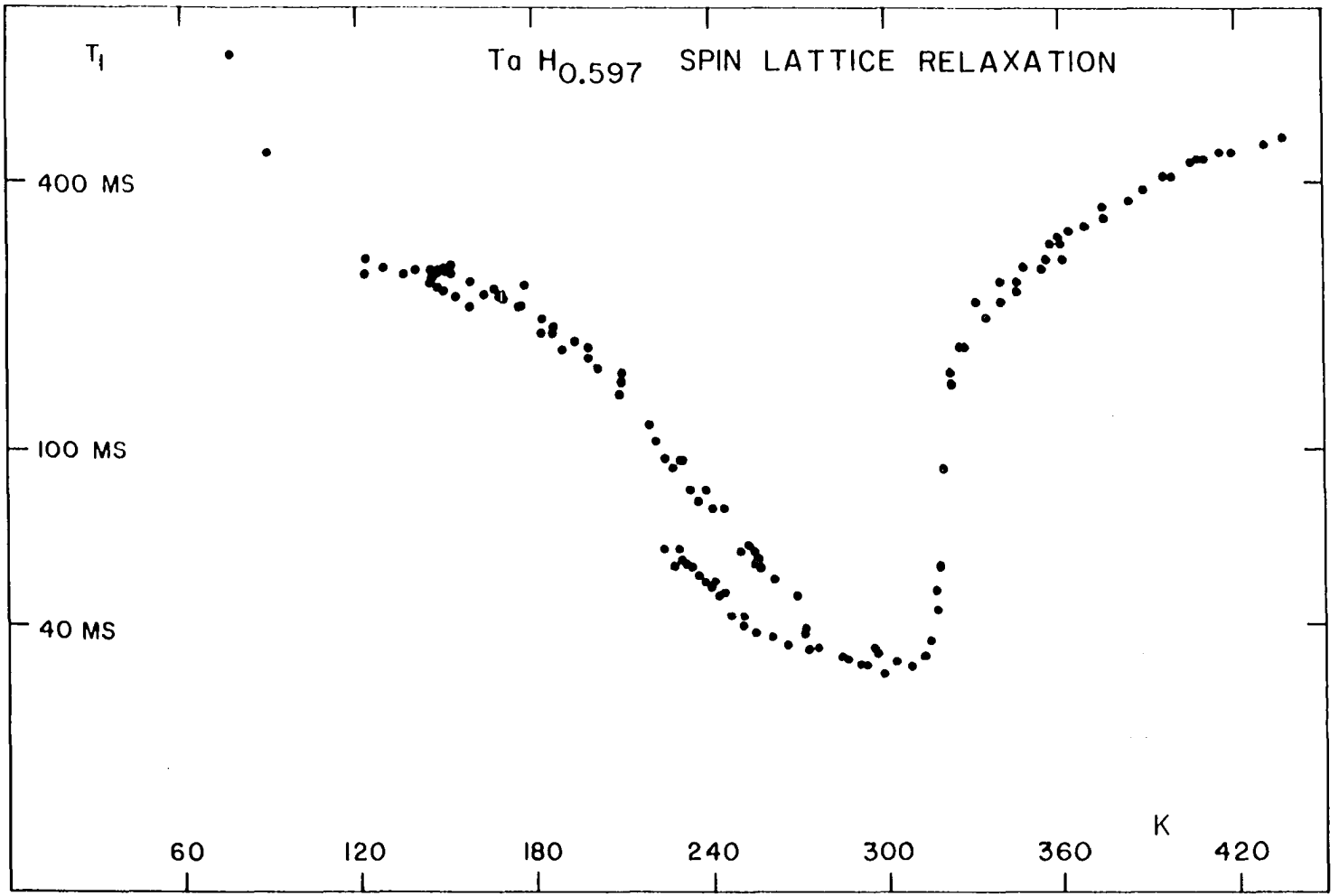

Figure 16. The proton spin-lattice relaxation time shows a hysteresis-like effect in the H/Ta 0.597 sample. The horizontal scale is in degrees Kelvin.

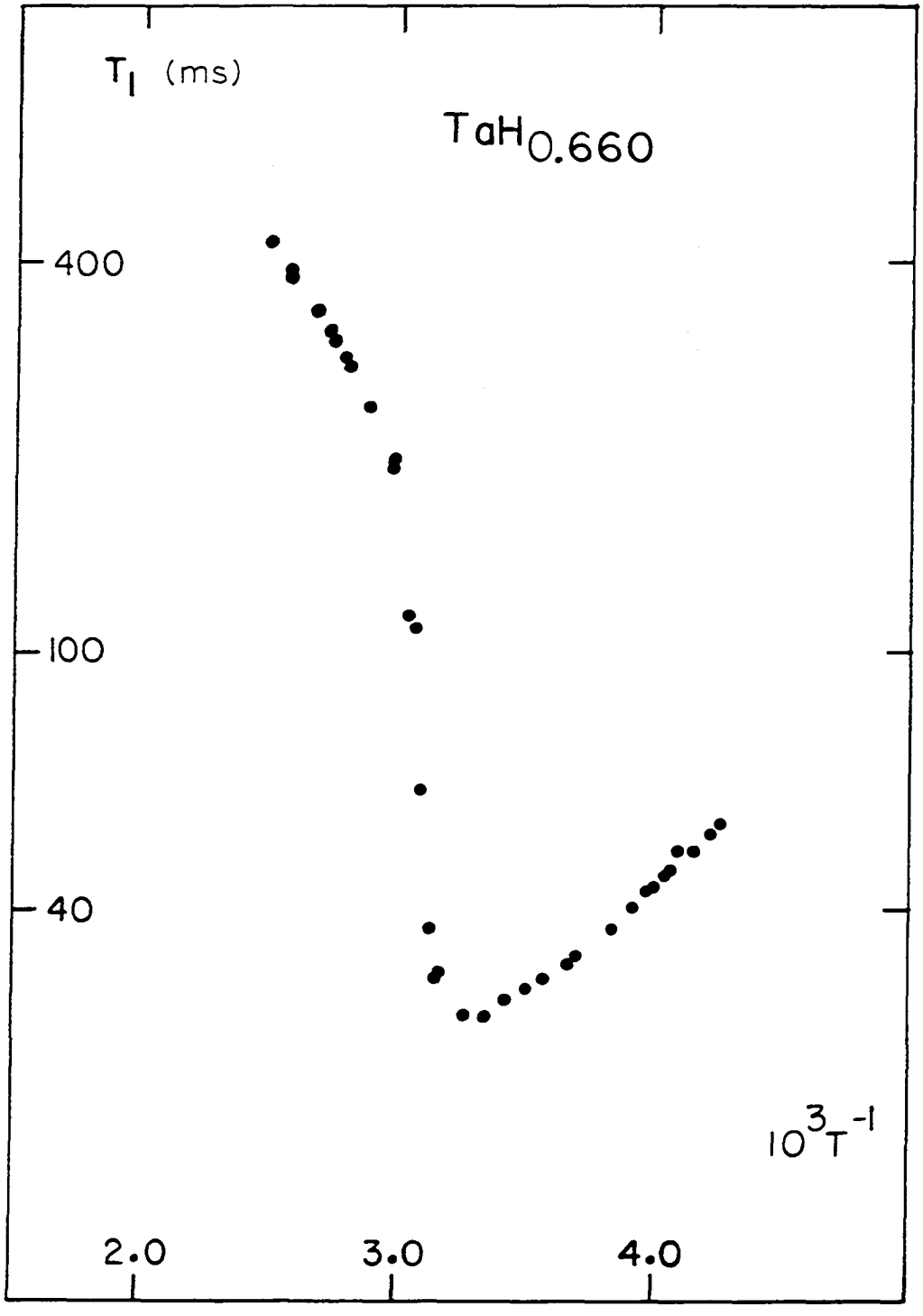

Figure 17. The proton spin-lattice relaxation time for the H/Ta = 0.660 sample.

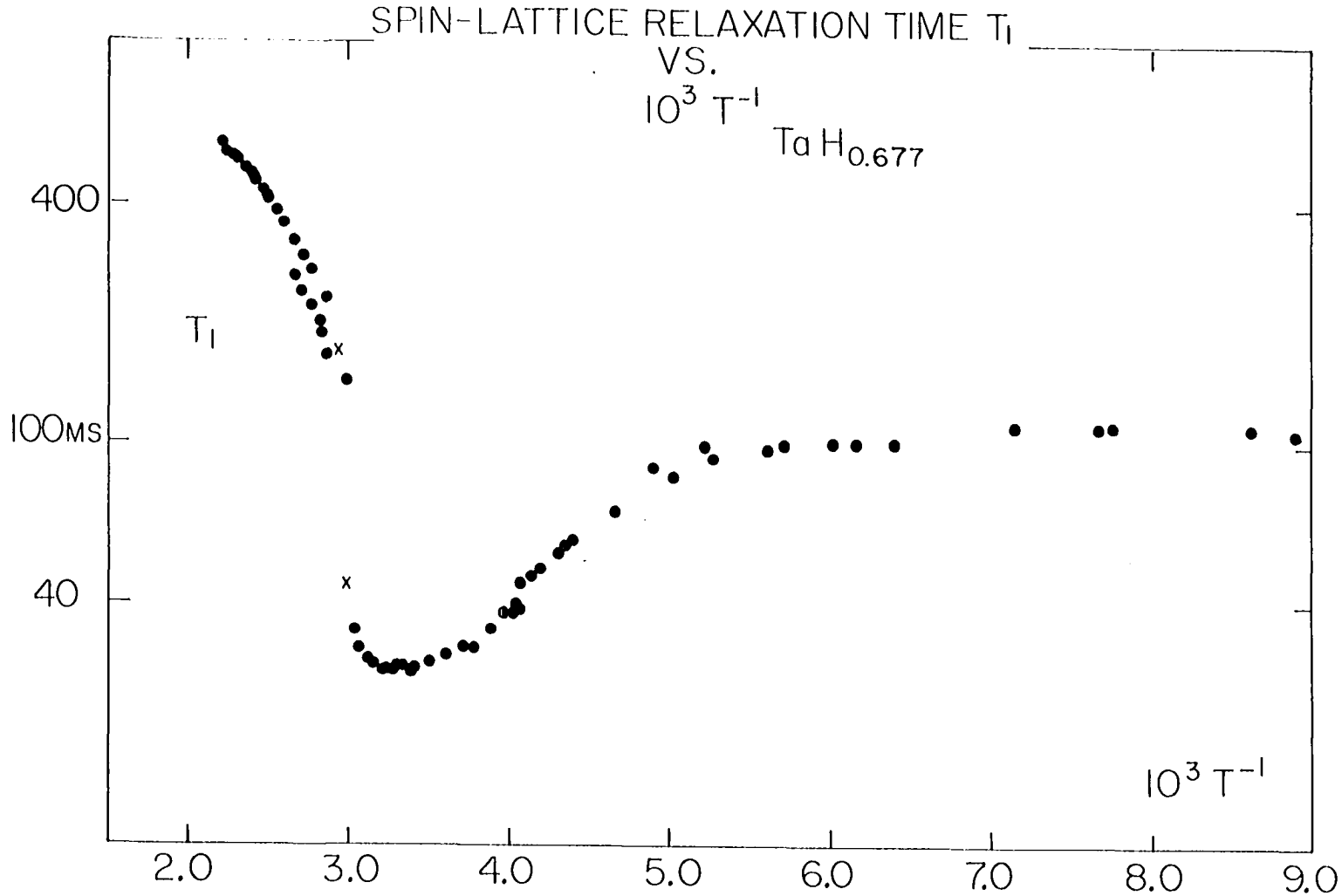

Figure 18. The proton spin-lattice relaxation time for the H/Ta 0.677 sample.

structural behavior. The remaining figures have inverse temperature as the independent variable because this is most appropriate for activated processes. In specific cases where more than one series of measurements were made at high temperatures, a variation of the value of the relaxation time was seen as sequential runs increased the value each time. However, the slopes and transition temperatures remained the same within the detection limits. The hydrogen content of the samples was determined to be x=H/Ta=0.155, 0.322, 0.486, 0.597, 0.660, and 0.677 as analyzed by A. Johnson and Dr. D. T. Peterson in the Metallurgy Division of the Ames Laboratory. The samples were prepared by Dr. A. S. Khan of the Ames Laboratory. The tantalum was prepared from Ames Laboratory tantalum, powdered, and hydrided by conventional techniques. Each sample was contained in a sealed glass tube. Special efforts were made to prevent oxygen and nitrogen contamination.

α Phase Data

In the α phase, relaxation rates are the result of two mechanisms which are comparable in strength. The diffusion of the protons through a cubic environment in a solid solution is the first of these mechanisms. The electron spin-nuclear spin contact interaction described briefly in Chapter IV is the other. Both of these mechanisms have predictable temperature dependences. A chi-squared search for the best fit to the three parameters of interest was done on the PDP-15 computer. These parameters are the activation energy, the prefactor of the activation

energy expression, and the T_1T or Korringa product. The fit did show certain flaws which indicated that not always enough temperature range was covered to achieve a limit at which one contribution clearly dominated. This shortcoming is included in the error estimates quoted in the table below.

Table 2. Reduced data from α phase

Sample H/Ta	T_1T constant (sec-K)	Activation Energy (eV/atom)	Prefactor Rate (10^{-2} sec^{-1})
0.155	116 ± 4	0.134 ± 0.006	0.8 ± 0.1
0.322	226 ± 15	0.133 ± 0.005	1.94 ± 0.10
0.486	330 ± 12	0.136 ± 0.005	2.40 ± 0.10
0.597	170 ± 10	0.144 ± 0.004	1.92 ± 0.18
0.660	2600 ± 100	0.142 ± 0.006	3.01 ± 0.20
0.677	1560 ± 300	0.143 ± 0.004	3.42 ± 0.20

Three very interesting conclusions can be drawn from this information. Despite some scatter in the results, the table gives a convincing presentation of the trends. First, the electronic contribution increases rapidly with decreasing concentration. This trend shows up in the better determination of the diffusion parameters at higher concentration with a correspondingly better determination of the Korringa constant at lower concentrations.

The electronic contribution comes from the mutual spin flip of an electron spin-nuclear spin pair when the electron has a finite probability density (s-like character) at the nuclear spin site. As mentioned in

Chapter IV Equation 29, the Korringa product of T_1T is proportional to the density of states at the Fermi surface or to the square of the bulk susceptibility. Stalinski (48), Ducastelle et al. (49), and Kazama and Fukai (46) all have published susceptibility versus hydrogen content data for the tantalum hydride system. As the hydrogen concentration increases, the susceptibility decreases rapidly until it has dropped a factor of four at 75 atom per cent. On the spin-lattice relaxation time plots, the electronic contribution becomes weaker (has a larger Korringa product) as the hydrogen content increases. This would indicate more electrons per metal atom as the concentration of hydrogen increases in accordance with the published susceptibility data.

The α phase activation energy is perhaps the most significant result of the fit. There appears to be a small trend toward higher activation energies (E_a) at higher concentrations but this is probably an artifact of the fit for the reasons mentioned above. The error bars quoted in Table 2 tend to substantiate this. A weighted average of the energies extracted yields a value of 0.1396 ± 0.0019 eV per atom. This is in excellent agreement with the accepted value of 0.140 eV which was measured only at low concentrations. Therefore, the activation energy does not seem to have a concentration dependence across wide ranges of concentration. Furthermore, using the fact that the T_1 minimum should occur at a temperature where the jump frequency is a fixed constant times the resonance frequency, the actual value of the jump frequency may be evaluated. Since the α to ordered phase or phases transition clearly changes some of the jumping character of the lattice, the positions of the minima in the

ordered phases cannot be used. However, because the structural changes are quite small, the value of T_1 at the minima should not change appreciably. Using the accepted value of the activation energy and the prefactor of the diffusional portion of the fit, the temperatures at which the minima occur can be computed. The results of this calculation show only a small spread of roughly 10 K about a value of 220 K. This indicates that the jump frequency or the correlation time does not change significantly throughout the concentration range measured. However, this does not imply that the diffusion coefficient does not change because the jump distance may change.

Structural Information

Structural information from these spin-lattice relaxation time measurements falls into three categories, the depth of the T_1 minimum, discontinuities in the slope of ln T_1 versus temperature or inverse temperature, and temperature regions where two-exponential relaxation is observed. By contrast to the α phase, the lower temperature ordered phases have restricted hydrogen occupation, and it therefore seems that the diffusion process may be quite different. This difference should appear as a discontinuity in the slope when the boundary from the ordered phases is crossed and as two exponential character of the decay whenever the α phase and an ordered phase co-exist. This point will be discussed later in some detail.

The strength of the hydrogen-hydrogen and hydrogen-tantalum contributions depends upon known spin constants and the sums of r^{-6}, where r is

the distance between the two atoms. In principle, this can provide a check on the structures proposed in the literature. However, the quadrupole interaction of the tantalum nucleus spreads its resonance over such a wide range of frequencies that its contribution to the relaxation Equations 26, 27 in the form of ω_s are no longer at any single frequency but rather a wide distribution of such frequencies ω_s. Still, the interaction is strong enough to add significantly to the relaxation rate. Figure 19 shows the results for the hydrogen-hydrogen interaction M_{HH} and the hydrogen-tantalum interaction M_{TaH} from calculations. The strength of the interaction is proportional to $(T_1 \text{ min})^{-1}$. The experimental data from the minima are roughly halfway between the least contribution possible, M_{HH} only, and the greatest possible, $M_{TaH} + M_{HH}$. No theoretical model seems adequate to explain this difference so that a good check on the occurrence of a given structure is not obtainable.

The remaining structural information, the signatures of α phase mixed with an ordered phase and the discontinuities in the data, are much more successful. At almost all phase boundaries observed, there was a two-exponential region evident in the data. In some cases, this was just the width of the transition and, in others, it indicated the co-existence of two phases in a true two-phase region. Figure 20 shows the characteristic signature of a two-phase region. If the components are not very different in relaxation times, or if one comprises less than about 10 per cent of the nuclei, then the two-phase signature may be difficult to distinguish. This accounts for the larger widths of transitions given by this study than by the Schober and Carl (8) results based on DTA. None-

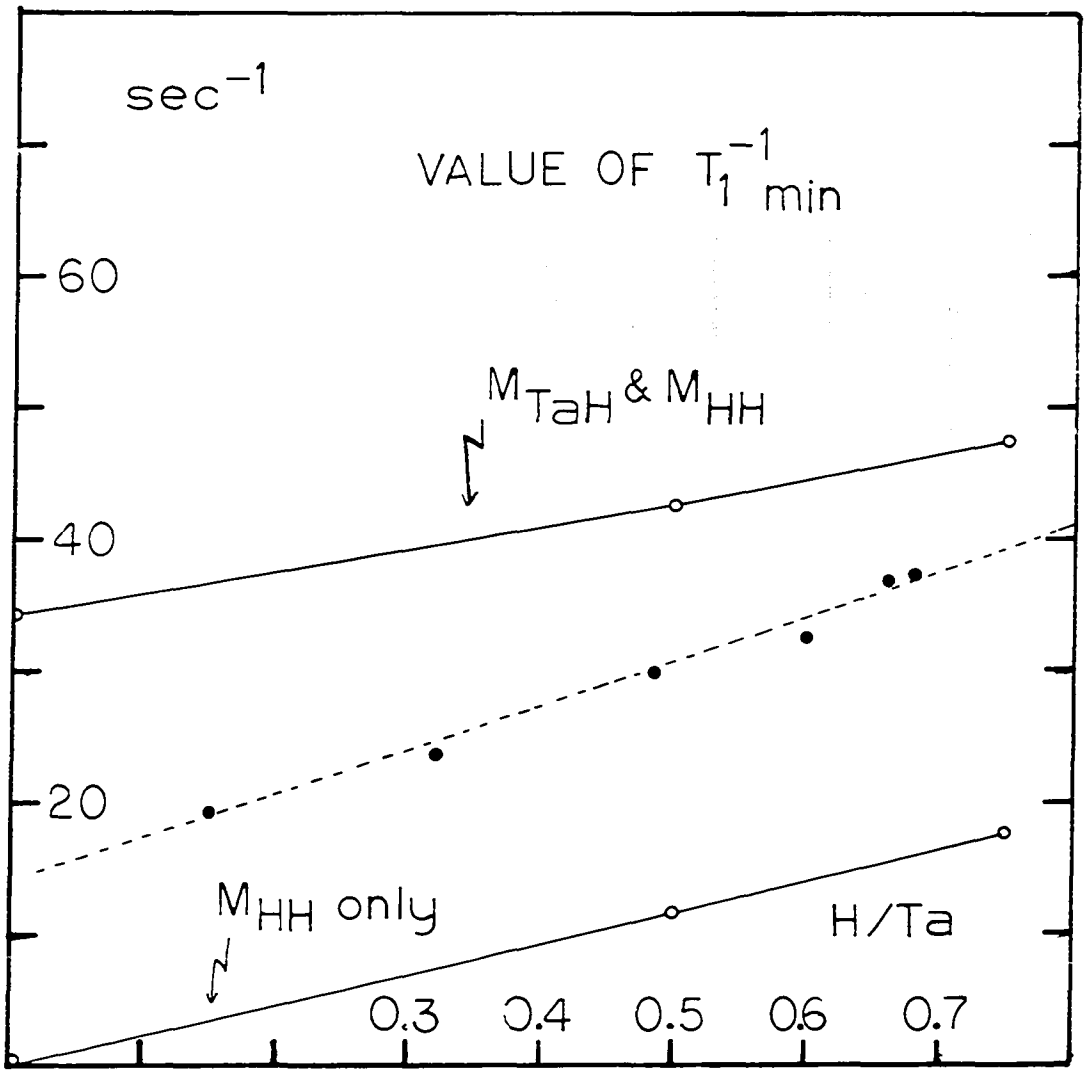

Figure 19. Calculated and experimental values of $(T_1 \text{ min})^{-1}$ are plotted versus hydrogen concentration. The value of the $(T_1 \text{ min})^{-1}$ is proportional to the local magnetic field strength at the hydrogen site. The lower solid line is the $(T_1 \text{ min})^{-1}$ value calculated with only the hydrogen-hydrogen local field strength, while the upper solid line includes the tantalum-hydrogen field strength (M_{TaH}) as well as the hydrogen-hydrogen contribution (M_{HH}). The experimental data are the solid dots along the dashed line.

Figure 20. The two exponential decay of the magnetization shown here is an example of the signature of a two-phase region.

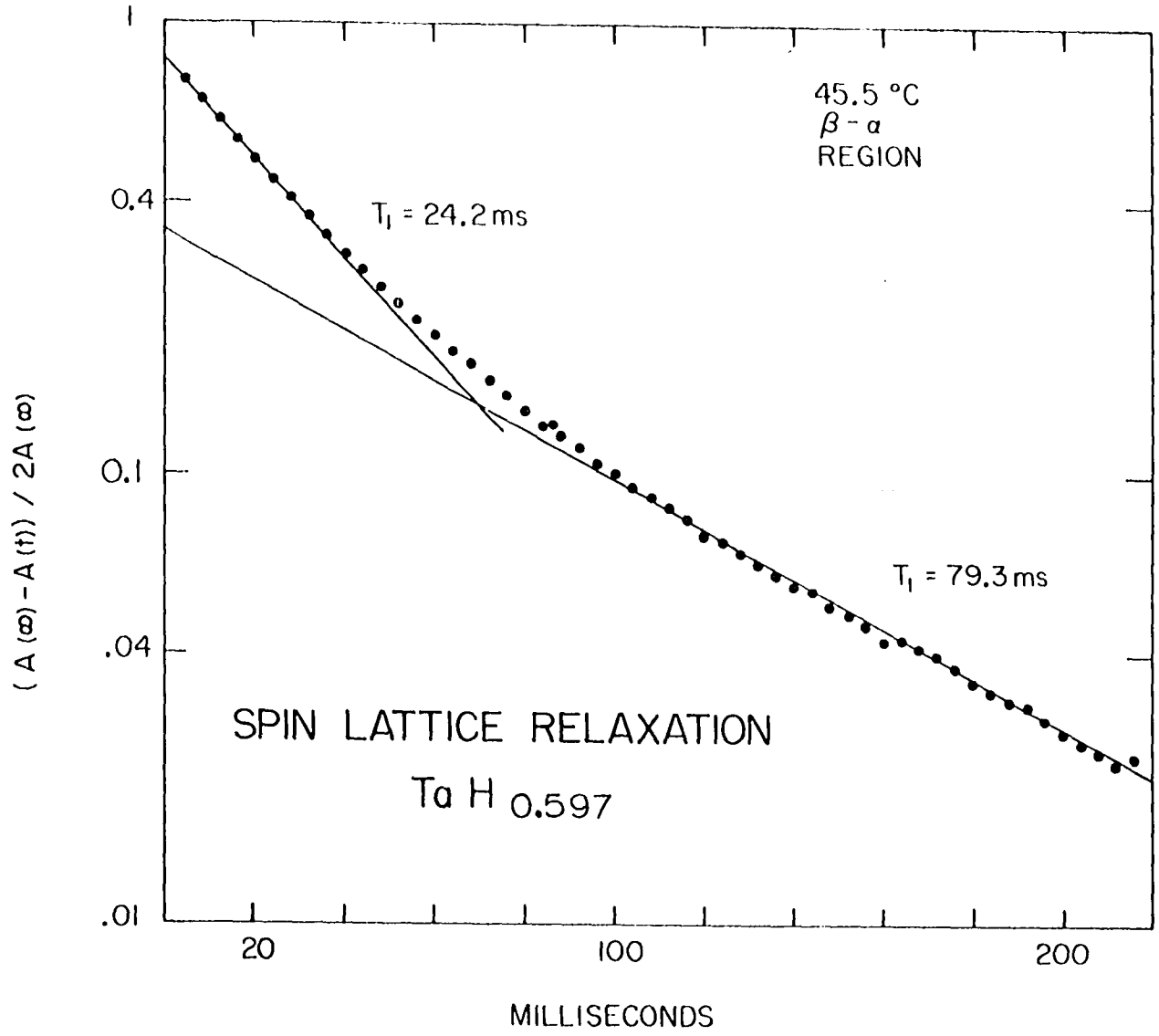
45.5 °C
β - α
REGION
T1 = 24.2 ms
T1 = 79.3 ms
SPIN LATTICE RELAXATION
Ta H 0.597
(A (∞) - A (t)) / 2A (∞)
1
0.4
0.1
.04
.01
20
100
200
MILLISECONDS

theless, conclusive confirmation of their α phase boundaries and two-phase regions is obtained. Figure 21 gives a superposition of the results from this study on the data and phase diagram of Schober and Carl (8). Table 3 has these phase boundaries numerically tabulated with errors and uncertainties listed. Since the samples were powders and therefore subject to inhomogeneities in hydrogen concentration, a differential thermal analysis instrument (Dupont Model 900) was used to verify that the phase boundaries and compositions were consistent with Schober and Carl. Showing excellent agreement, these measurements conclusively demonstrated that the relaxation time effects were indeed associated with phase boundaries. The following section describes the results in Table 3 on a sample-by-sample basis.

Structural Behavior of the Individual Samples

At this point, the structural transitions found are discussed in some detail. The results of Schober and Carl, and the NMR and DTA results contained in this study are compared. Special attention is given those samples which illustrate points which are examples of material for later discussion. In particular, it appears that the mechanism that allows one to observe the phase boundaries with NMR is a change in the host lattice which modifies the diffusion process. This means that the ordered phases probably cannot be distinguished from one another, but can be distinguished from the α or ϵ phases. Where this mechanism is most apparent, the discussion will emphasize that point.

Figure 21. The phase transitions determined by pulsed NMR are superimposed upon the phase diagram of Schober and Carl (8). The arrows indicate the extent of two-phase regions detected by NMR by the characteristic shown in Figure 20.

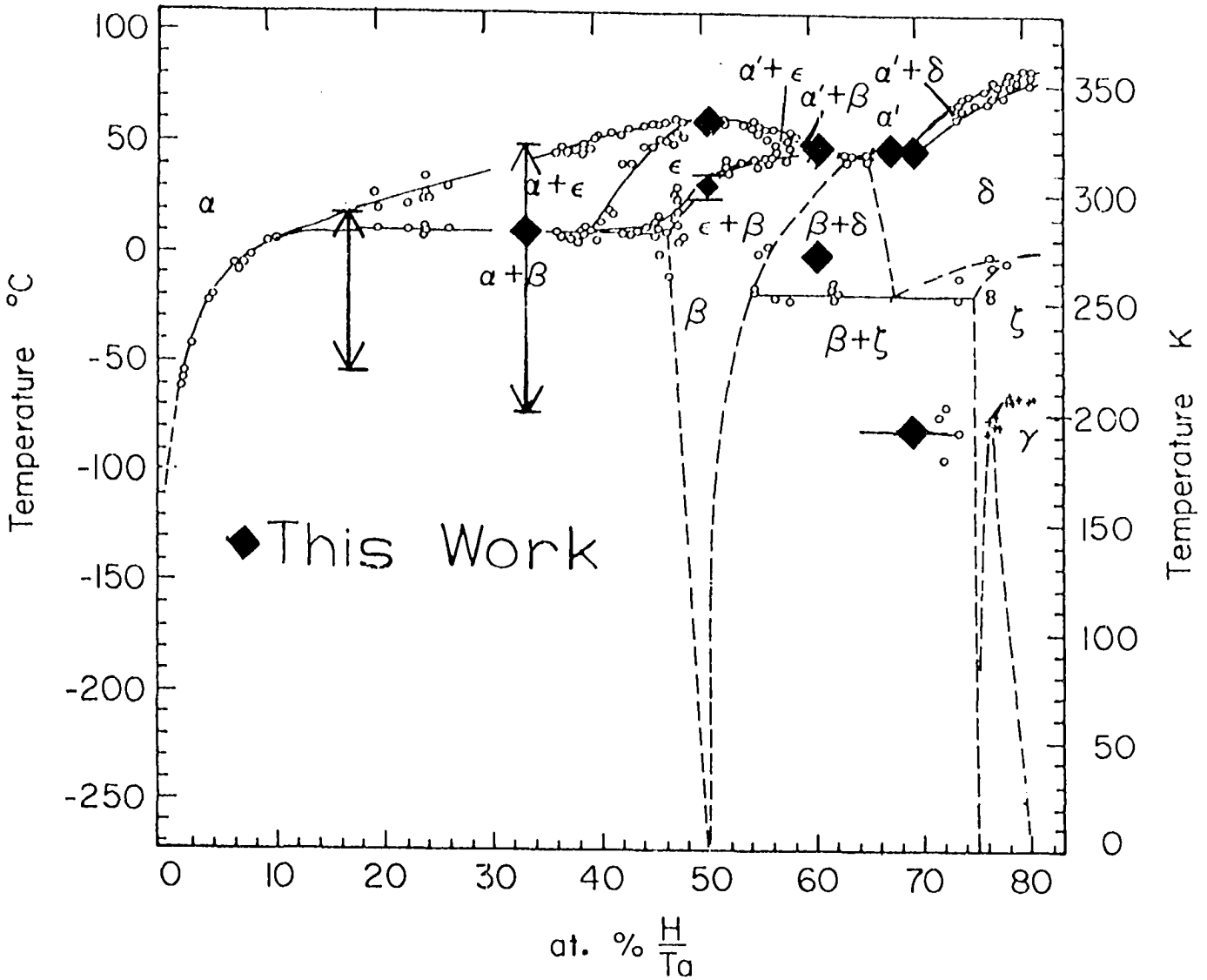
Temperature °C
Temperature K
at. % H/Ta
This Work
α
α+ε
α+β
ε
ε+β
α'+ε
α'+β
α'+δ
α'
δ
β
β+δ
β+ζ
ζ
γ
100
50
0
-50
-100
-150
-200
-250
350
300
250
200
150
100
50
0
0
10
20
30
40
50
60
70
80

Table 3. Transitions measured for Ta-H system

H/Ta	NMR Transition Temperatures	DTA Transition Temperatures[a]	Schober and Carl Identification
0.155	-60 to 23 C	only broad indication	$\alpha+\beta$ to $\alpha+\epsilon$ to α
0.322	5 to 55 C[b]	35 ± 13	$\alpha+\epsilon$ to α
	-73 to -13 C[b]	no data	$a+\beta$ to $\alpha+\epsilon$
0.486	60 ± 4 C[c]	58 ± 1 C	ϵ to α
	34 ± 2	34 ± 1 C	β to ϵ
0.597	45 to 51 C[c]	43.5 ± 1.0 C	β to $\epsilon+\beta$
		41.0 ± 1.0 C	$\epsilon+\beta$ to α
0.660	45 to 61 C[c]	47 ± 1 C, width 3 C	$\beta+\delta$ to $\alpha+\beta$
		49.5 ± 1.0, width 3 C	$\alpha+\beta$ to α
0.677	45 to 63 C[c]	58 ± 1 C, width 8 C	δ to α

[a]No DTA measurements were taken below 22 C.

[b]Two exponential behavior was clearly observed showing a two phase region.

[c]Two exponential behavior was observed in transition region.

The lowest concentration studied was the x=0.155 sample. A transition was found over a wide region from -60 C to 23 C, corresponding to an $\alpha+\beta$ to α transition. There was no multi-exponential spin-lattice relaxation observed for this sample. Because of the low hydrogen concentration, the signal was weak, and no signal was observable below the lowest temperatures depicted here in Figure 13. DTA results only indicate the impression of a weak, wide transition. Sample inhomogeneities may be at the center of this problem. The electronic contribution is quite strong for this concentration as well, so that it may mask any differences in the diffusional contribution. This is qualitatively shown by the fact that no distinct diffusive minimum is apparent. It should also be noted that the end points of the data regions used for the transitions are somewhat arbitrary and that the widest interpretable region has always been used.

Covering the α to $\alpha+\epsilon$ and the $\alpha+\epsilon$ to $\alpha+\beta$ phase changes, the temperature dependence of T_1 in the x=0.322 sample showed wide regions which the two-exponential character indicates are two phases co-existing, as the phase diagram indicates. As shown in Figure 14, the diffusive contribution is dominant enough to make this determination possible. The NMR data show a two-phase region from 5 to 55 C in rough agreement with the DTA which showed a large spread about 35 C. Although there was no DTA data available below room temperature, the NMR relaxation data revealed another two-phase region which was consistent with Schober and Carl. This region ends at a low temperature apparently when both phases begin to show

the same diffusive behavior. An alternate possibility is that another phase boundary is crossed, but there are no reported phase changes in this temperature region.

Perhaps the richest sample in terms of structural phase transitions is the x=0.486 sample. From the Schober and Carl diagram, the sample is in the pure β phase at low temperature, and then passes through a narrow two-phase region into the pure ϵ phase. Once again, a transformation occurs to the α phase as the temperature is increased. As the temperature is increased from 220K, there is an inflection point in the slope of T_1 vs. T at 294K as shown in Figure 15. This does not correspond to any observed phase boundary. Matching the β to ϵ transition well, there is a sharp drop to a minimum at 34 C, which is confirmed by the DTA measurements. The subsequent increase in T_1 with temperature is noted as having slight non-exponential character, possibly reflecting the DTA result which detects two transitions within two degrees. A pronounced increase in T_1 takes place in the region from 50 C to 60 C, which includes the narrow two-phase region within it. A DTA scan covering the entire range is shown in Figure 22. The T_2 measurements show the same behavior and also help demonstrate the diffusional nature of the relaxation mechanism. This is the most conclusive sample for the argument that the α, ϵ, and ordered phases differ in the environmental effects at the hydrogen sites of the differing tantalum lattices, and that this difference influences the diffusion of the hydrogen atoms. This argument also agrees

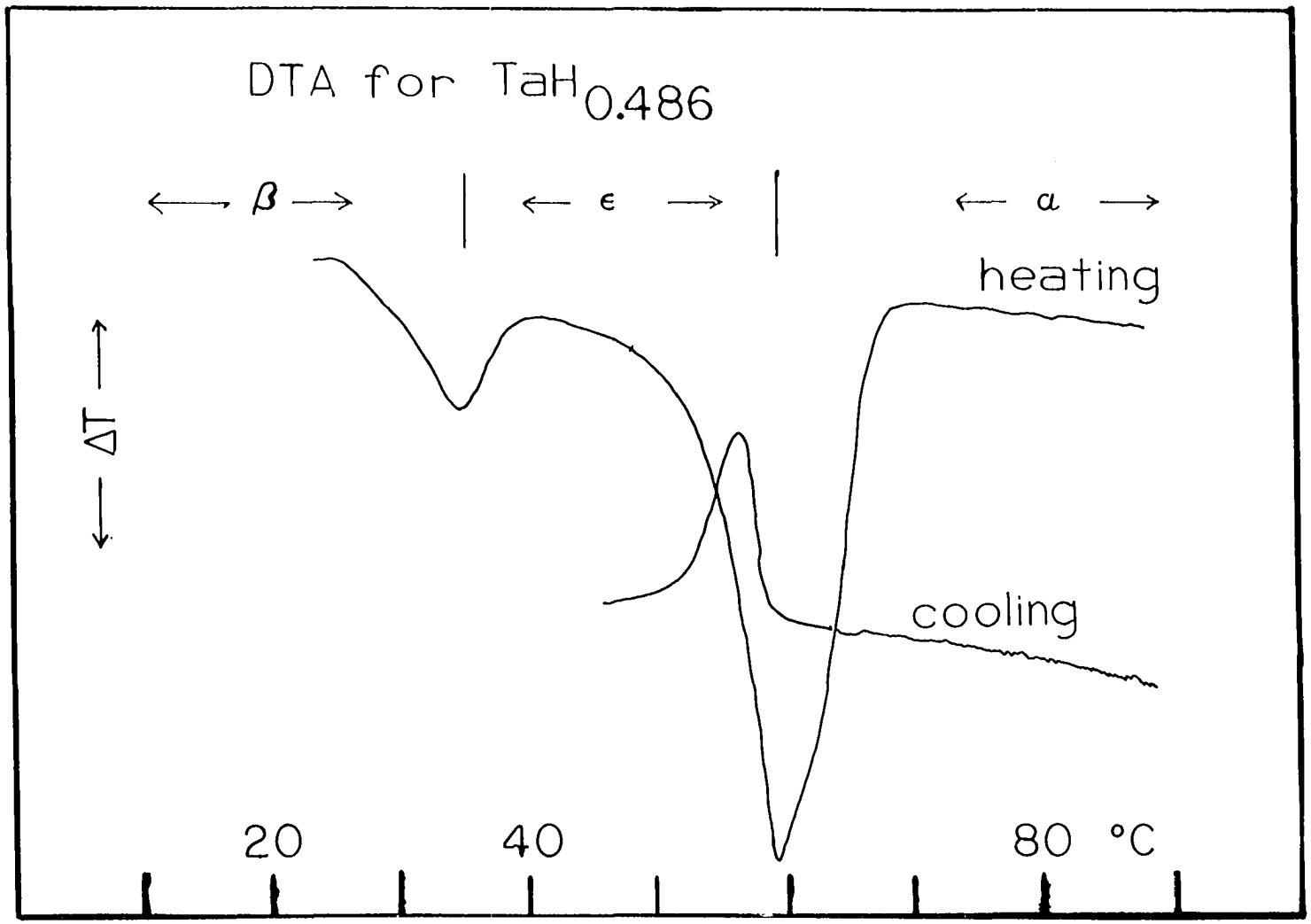

Figure 22. Differential thermal analysis confirms the structural phase transitions for the H/Ta = 0.486 sample.

with Schober and Carl who claim the ϵ phase is different from either the cubic or the face-centered orthorhombic structures, and is possibly tetragonal.

The remaining three samples have ordered phases exclusively at lower temperatures, and high temperature phase boundaries exist in an eutectic region of the phase diagram. Figure 23 shows this region from Schober and Carl with the pulsed NMR transitions plotted on it as well.

The first of these samples is the x=0.597 sample for which the NMR relaxation times show a high temperature transition from an ordered phase to the α phase between 45 and 51 C. This agrees quite well with a β to $\alpha+\epsilon$ to α series of phase changes. The DTA measurements made on this sample show transitions at 41 and 43 C, somewhat lower in temperature than expected. As yet, no good explanation exists for this discrepancy. At -3 C and below, there is evidence for an additional phase change from a hysteresis-like effect in the T_1 data. However, since all of the data were obtained by heating the sample from lower temperatures, this is not a true hysteresis. The essential difference between the two T_1 curves (see Figure 16) is that the curve with the higher T_1 values was obtained by cooling to 77 K and taking measurements during a heating run, whereas the other (lower) curve was also measured with a heating run from approximately 200 K. It should be noted that while the upper and lower curves did coincide at 271 K, there is no low temperature termination to this anomalous divergence. Also, while there is evidence from Schober and Carl of phase transitions occurring in the vicinity of 250 to 260 K, direct agreement is lacking.

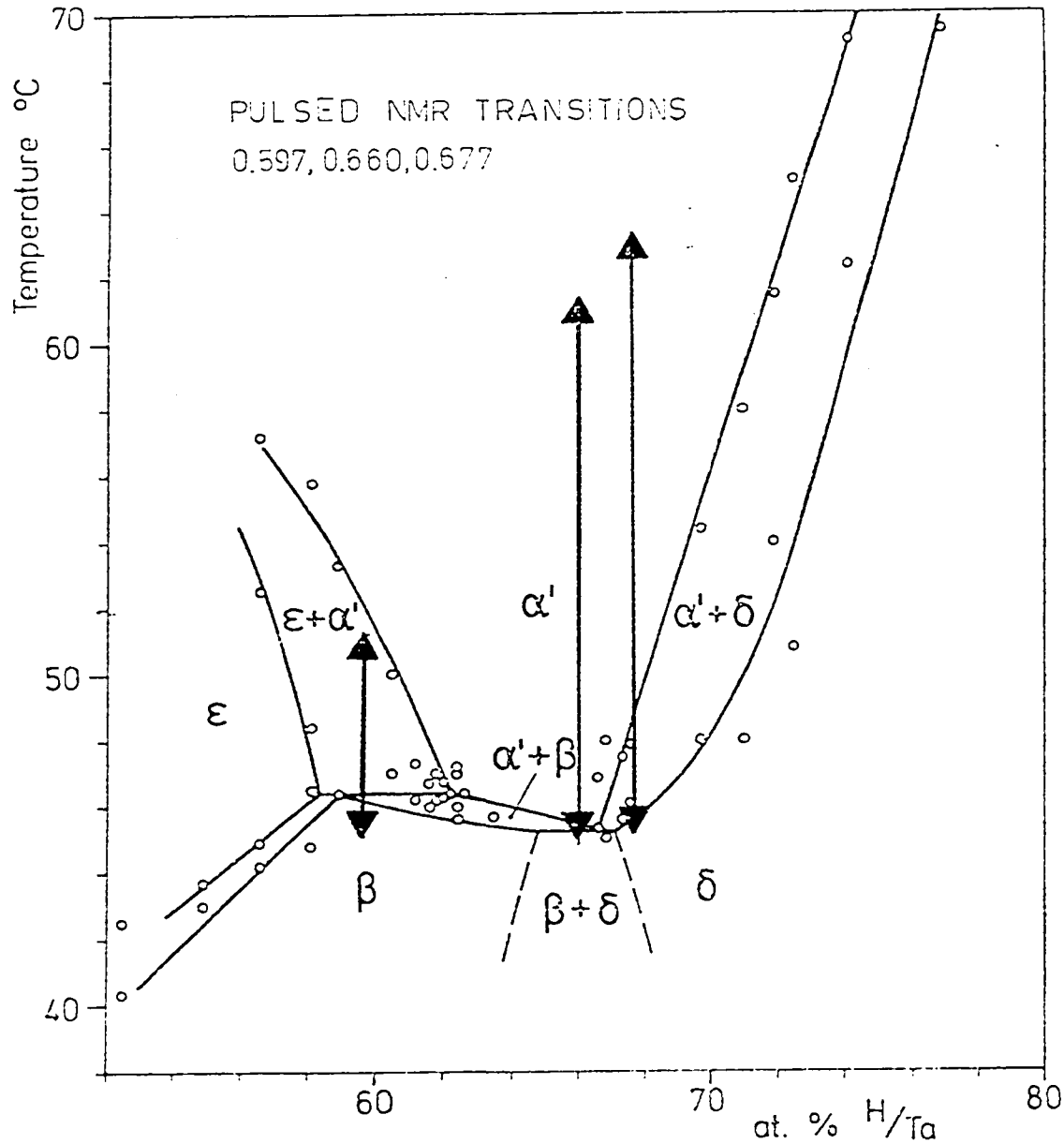

Figure 23. The phase transitions determined by pulsed NMR for the three high hydrogen concentration samples are superimposed on an expanded diagram by Schober and Carl (8). The great extent of the transition region based on the NMR data (indicated by the arrows) is believed to arise from concentration inhomogeneities.

The samples x=0.660 and 0.677 are so close in composition that only the x=0.677 sample was measured over the entire temperature range. Both samples were run in the high temperatures region to locate the α phase boundary. The data for these samples is shown in Figures 17 and 18. The data from the NMR transitions are also plotted in Figure 23 and agree well with Schober and Carl. The rather large ranges compared to Schober and Carl can be ascribed to the inhomogeneities in the composition. which may overlap into the steep variations away from the eutectic region. This is also evident in the DTA results quoted for these samples in Table 3. The 0.677 sample yielded data showing the effect of the thermal cycling in the high temperature region plotted. The 0.660 sample was run continuously throughout the α phase region without returning through the α phase boundary. This procedure eliminates the double-valued slopes sometimes seen on several runs through this range.

Although this investigation does not improve on the accuracy of the work of Schober and Carl, it certainly verifies the α phase boundaries and the existence of the ϵ phase as a host lattice structure differing from either of the two known tantalum lattice structures. The verification of the ϵ structure difference is primarily from the two exponential decays visible in the $\alpha+\epsilon$ regions of the x=0.322 sample and in the marked transitions between the β, ϵ, and α phases seen in the x=0.486 sample. It is also interesting to note that this two-decay behavior does not occur above x=0.5 and below the α to ordered phases transition. Several unresolved questions remain in the structural analysis presented here. First, the cause of the thermal cycling effects may perhaps be the

fracturing of crystallites as the non-cubic phases are entered from above, but this has not been verified by sequential checks of particle size. The hysteresis-like effect on the 0.597 sample was checked in the course of several runs, but this was never found in any other sample measured. Nor does this seem to agree with any known transition in hydrogen ordering at low temperatures. Precautions were carefully taken to avoid any systematic errors in the measurements, especially as regards the measurement of the equilibrium magnetization (see discussion in Chapter V on experimental criteria). The only speculation offered at this point is that different initial cooling procedures must leave the sample in different phases from which heating produces different effects. It should also be noted that inflection points in the slope of T_1 occur in all but one of the samples at approximately 200 K. These are probably not structural transitions at all, but rather manifestations of the low temperature diffusion processes discussed in the next section.

Relaxation in the Non-cubic Phases

Spin-lattice relaxation times can give two separate pieces of information about the diffusion process. Figure 5 in Chapter IV outlines the expected relaxation times for an activated motional process. The slopes away from the minimum in T_1 are proportional to the activation energy, whereas the minimum itself identifies the temperature at which the jumping rate is equal to the resonant frequency times a constant on the order of unity. Under ideal circumstances, the shape of the minimum as well as the slopes can give an accurate measurement of the activation energy, if the

assumed spectral density function of the motions is correct. From the previous discussion of the value of the minimum, it was seen that the tantalum-hydrogen contribution is not well-enough understood to completely characterize the fitting function. Nonetheless, the reduced jump frequency, y, should stay within a comparatively narrow region at the T_1 minimum as given below

$$1.6 < y \equiv \nu/\omega_o \equiv 1/\omega_o\tau_c < 2.0. \qquad 32$$

If only the hydrogen-hydrogen interaction were taken into account, the value of y at the T_1 minimum would be 1.6. The tantalum-hydrogen contribution should be centered about 2 since the residence time of the hydrogen is twice as long near a tantalum as when near another hydrogen. Calculations using the spectral density function given in Equation 28 in the relaxation equation (Equation 26), show the reduced frequency at the minimum to be close to 1.85. This was derived using the extracted value of the tantalum-hydrogen interaction strength and assuming the calculated value of the hydrogen-hydrogen interaction and the experimental total value. Although the tantalum-hydrogen portion is not as large as calculated, it is nearly equal to the hydrogen-hydrogen contribution. Figure 24 illustrates the temperature dependence of the T_1 minimum versus concentration. All of the minima occur in non-cubic phases, except for the 0.322 and 0.155 samples which are in the mixed $\alpha+\beta$ region. Several interesting conclusions can be drawn from this information. First, the three samples in the ordered phases (0.677, 0.660, 0.597) are quite close in their temperatures at the minimum indicating that the absolute value of the jump frequency does not change noticeably through these

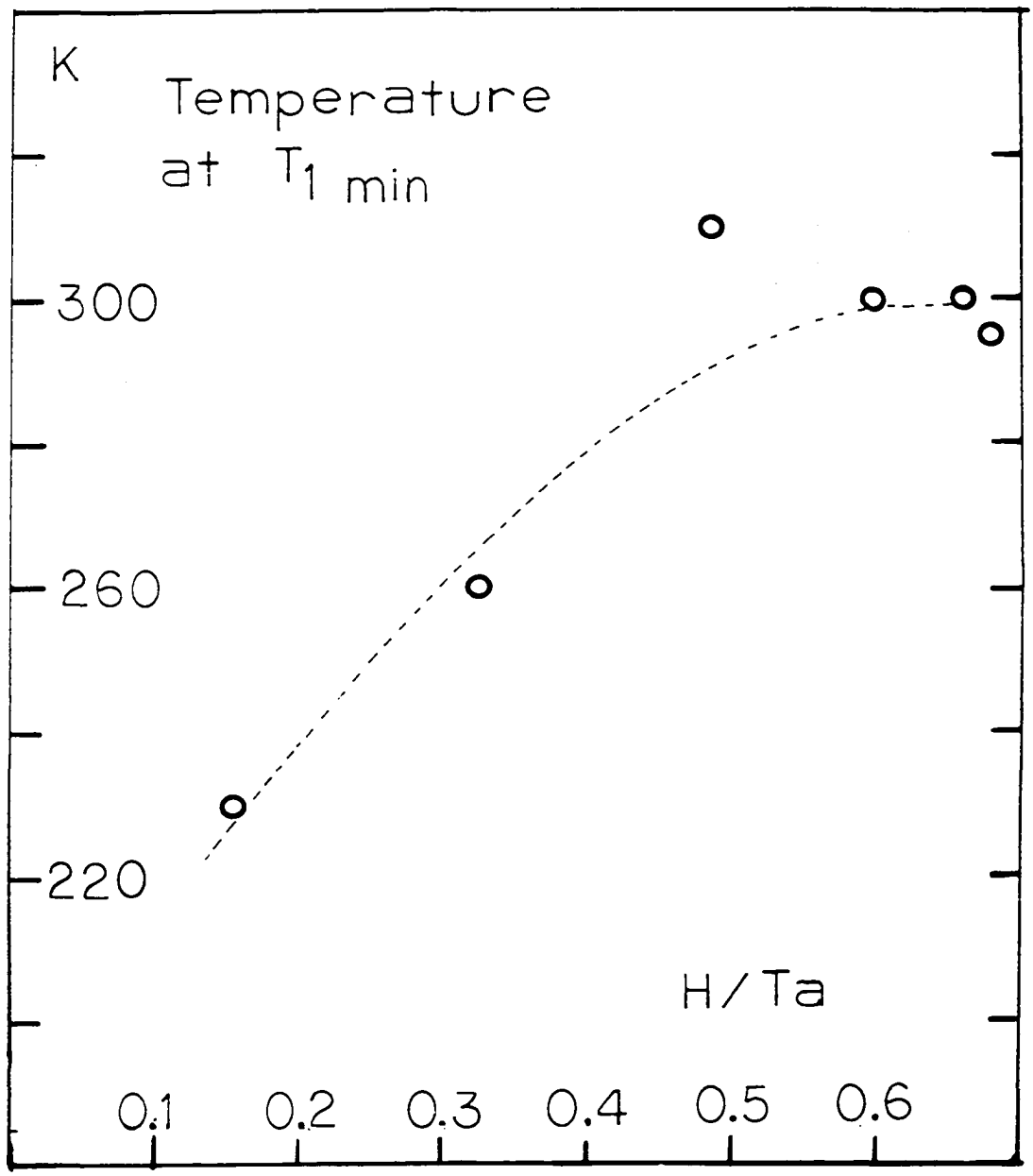

Figure 24. The minimum in T_1 occurs when the jump rate of the hydrogen is comparable to the Larmor frequency. The temperature at which T_1 is a minimum provides a means of extracting the value of the jump rate.

regions. The ϵ phase sample ($x = 0.486$) has a higher temperature at the minimum than any of the others. Since there are a great many phase boundaries at this composition one might suspect that the actual minimum had not been reached before a phase change to the β phase had occurred. However, the value of the minimum is quite close to the remaining experimental points for the minima shown in Figure 19. The calculation of the α phase behavior leads to an estimate of 220 K for the minima if no phase change occurred. So then, one can qualitatively state that the jump frequency is fastest in the α phase, and slows by a factor of approximately 7.2 if a uniform activation energy of 0.140 eV/atom is assumed. Diffusion in the ϵ phase is apparently even slower, although the data for this is very limited. Although the two lowest composition samples do not have indisputable minima, the important factor is that they follow these assumptions with a decrease in the temperature of the T_1 minimum as concentration decreases.

An alternate possibility exists, however. This is simply that the nature of the contributions to the minimum may change in their relative intensity, thus shifting the value in the range of Equation 32. In fact, the calculated values based on the simplest arguments would give such a trend. However, the experimental results show that the contributions are very nearly equal across the entire composition range studied as shown in Figure 19.

Anomalous Relaxation in the Low Temperature Regions

It is interesting to note that the T_1 behavior in the low temperature phases does not resemble the predicted curve shown in Figure 5. The large regions at lower temperatures (higher $10^3/T_1$) where the relaxation is nearly constant or is rising very slowly are quite different than expected. Although all of the samples show this behavior to some extent, the highest concentration x=0.677 sample shown in Figure 18 is the most striking. Because Figure 16 is graphed linearly with temperature, the low temperature increase in T_1 can be included on this graph. For the remaining data plots, the increase is not visible because of the inverted temperature scale. Table 4 quotes the values for all of the samples at the liquid oxygen and liquid nitrogen temperatures respectively.

Table 4. T_1's at low temperatures

Sample H/Ta	T_1 at 90.3 K (ms)	T_1 at 77.4 K (ms)
0.155	no signal observable	
0.322	664 ± 7	683 ± 12
0.486	569 ± 7	745 ± 7
0.597	468 ± 2	790 ± 11
0.677	278 ± 2	554 ± 6

These measurements are germane to many arguments presented here. In addition, the definite rise of T_1 in the 0.677 sample rules out such possibilities as relaxation by paramagnetic impurities which would cause T_1 to continue to be flat (50). Another possibility that is eliminated by low temperature data is that the Korringa electronic contribution has increased

its relative strength. The low temperature trends do not fit this model at all since the T_1's should double over the flat region in the 0.677 sample, and do not rise rapidly enough to account for the behavior at the lowest temperatures. Nor can a phase change be convincingly used to explain this anomalous region in T_1, since one might expect a discontinuity in the slope of T_1 versus inverse temperature but not a long constant region. The problem also involves a concentration dependence which is quite interesting. Although the data does not extend to low enough temperatures, trends can be seen which indicate the general behavior especially with the use of the data in Table 4. As the concentration increases, so does the strength of the anomalous interaction. However, the region where this interaction weakens on the low temperature side of the minimum is higher in temperature with increasing hydrogen concentration.

Two qualitative explanations exist for the anomalous low temperature relaxation. First, there is the possibility of a complicated diffusion effect contributing to a much different spectral density function for the motion than that assumed in Equation 28. Secondly, one may postulate a cross-relaxation of the hydrogen with the tantalum nuclei which have quadrupole-like splittings instead of the simplified Zeeman levels. Both models have some difficulties and some very believable features, but neither can be well-enough substantiated to be conclusive.

Multi-Step Diffusion Model

The first model assumes that the diffusion differs from the usual isotropic, activated mechanism. This is certainly reasonable because

Roenker et al. (12) found that in the ordered phases restricted diffusion occurred in an ordered plane. The structural information available (11) also confirms this point of view. Indeed, a very similar model was proposed by Fukai and Kazama (47) to explain anomalous diffusion in the vanadium hydride system. The model contains the idea that the actual jump of the hydrogen may hesitate in an intermediate site (in this case an octahedral site) before continuing to the next tetrahedral site. The intermediate site might then be metastable in energy and require only a small fraction of the first jump's energy to continue. Clearly, if this were true, the attempt frequency of the jumps from the metastable site would be higher. The result of all this complication would be to add a second contribution to the spectral density function with a higher attempt frequency and lower activation energy. This should appear in T_1 relaxation time data as a second minimum centered at lower temperatures. Furthermore, the slopes away from this minimum should reflect the lower activation energy and spread this contribution's minimum over wide ranges of temperature. One might further postulate that the relative strengths of the two mechanisms might become equal when the concentration increases because the hydrogens might jump to the intermediate site and then be repelled if the next site is occupied. Clearly, if this happened, it would happen more often as hydrogen content increased. The x=0.677 sample shows the trends most definitely and serves as the best example of them. In this sample, the slope away from what is postulated as the second minimum is 0.05 eV/atom on the low temperature side, quite a low activation energy, indeed.

Qualitatively at least, this model can fit the data. Fukai and Kazama (47) report the second energy in the vanadium hydrogen system to be almost equal to their larger activation energy. In the vanadium case, the hydrogen is known to occupy the octahedral sites 90% of the time and tetrahedral sites 10% of the time, so that this model is at least reasonable for vanadium. In the tantalum case, the hydrogen seems to occupy tetrahedral sites exclusively. However, the argument shows the hydrogen in tantalum to have a shorter correlation time in the intermediate site (larger jump frequency from it), so that hydrogen residence in these sites may not be observable. In principle, the fact that the total spectral density must be normalized should decrease the calculated depth of the minimum because of the additional contribution.

Cross-Relaxation Model

The second model assumes that the isotropic spectral density function is at least qualitatively correct, and postulates that the anomalous relaxation comes from cross-relaxation to the quadrupole levels of the tantalum nuclei. The process involves the mutual spin-flip of a tantalum nuclear spin and the hydrogen nuclear spin which is observed in the experiment. Instead of Zeeman levels for the quantization of the tantalum nuclei, the quadrupole splitting should be dominant with a value of approximately 60 MHz. This splitting was calculated by using the measured niobium quadrupole resonance and scaling for the much higher tantalum quadrupole moment. In point of fact, the tantalum should also be split into further levels by the Zeeman interaction which would be a weak perturbation. Then, according to the processes outlined in Table 1, the

frequency of the tantalum resonance would be essentially its quadrupole frequency instead of its Larmor frequency. The axis of quantization would be along the largest of the internal electric field gradients, which in a powder will occur in many orientations with respect to the applied magnetic field. This will cause a distribution of tantalum frequencies. By contrast to the previous model, only one spectral density function is postulated instead of two, but it would be sampled by the tantalum-hydrogen interaction over a distribution of frequencies about the hydrogen resonance frequency. When the temperature neared a range where this distribution of frequencies sampled by the hydrogen through interaction with the tantalum spin neared the jump frequency of the hydrogen an increased relaxation rate would occur. If, however, the tantalum quadrupole frequency approximately equalled the hydrogen Larmor frequency, very fast relaxation should result (51). These effects do not seem to occur in this sample, however.

Once again, the model seems to fit the relaxation time data in a qualitative fashion. The α phase should avoid the problem because the cubic symmetry would destroy the large electric field gradients and bring the tantalum splittings into the purely Zeeman regime. However in fact it has thus far been impossible to detect the ^{181}Ta NMR even in the cubic α phase (12), indicating that there still exists a very substantial inhomogeneous quadrupolar broadening of the tantalum Zeeman levels despite the nominally cubic symmetry. The model offers no way of predicting the concentration dependences or the relative strengths unless the tantalum resonance pattern can be measured. This is primarily because the number

of electrons available to screen the hydrogen (and thus change the electric field gradients) is not known. The model does solve the problem of the strength of the hydrogen-tantalum interaction at the T_1 minimum by simply claiming the tantalum resonances spread this strength over a wide frequency range.

Unfortunately, because measurements could not be extended below 77 K, there is not enough data to conclusively establish either model. A very similar relaxation at low temperatures was observed by Fukai and Kazama (47) for the vanadium hydride case and was also modeled as a multi-step motional process. Since the pure quadrupole frequency of ^{51}Va is a factor of about 100 smaller than ^{181}Ta, the quadrupole cross-relaxation model should not be applicable to the vanadium hydride system. However, while there is evidence for the occupation of two sets of sites in the vanadium-hydrogen system, the hydrogen is observed to occupy only tetrahedral sites in the tantalum hydride case. Still, the multi-step diffusion model seems to have more physical evidence in its favor, i.e. the restricted diffusion seen by Roenker et al. (12) and the occurrence of the same phenomenon in the closely parallel vanadium hydride case.

Spin-Spin Relaxation

The spin-spin relaxation times measured in this experiment do not follow the predicted behavior for activated motions except in a very qualitative sense. As mentioned in Chapter IV, the spin-spin relaxation time T_2 is much more sensitive to changes in the local fields throughout the lattice than T_1. The non-zero susceptibility of the samples also contributes to a distribution of gradients to the local fields as well.

Measurements by Wayne and Cotts (52) showed that limited path length would also alter the relaxation time if the distance traveled in the time T_2 was comparable to the particle size. Changes consistent with either of the two models proposed for the low temperature anomalous relaxation would also be reflected in T_2. Preliminary measurements of T_2 for this study showed several anomalous features. The measured T_2's from the spin-echo experiment, the Carr-Purcell (CP) sequence and the Carr-Purcell-Meiboom-Gill (CPMG) sequence all yielded increasing values by factors of two to ten respectively. Furthermore, some echo modulation effects are observed in the CP and CPMG sequence measurements. The T_2 results reported in Figure 15 are CPMG echo trains which have been fit by a single exponential. Although T_2 increases rapidly from its low temperature local field strength limit as expected, it becomes constant at about the transition into the α phase instead of increasing with T_1. Since the value of T_2 cannot be unambiguously measured, consistent interpretation of the data is difficult. In addition, CP and CPMG echo trains often show modulation of the decay curves and an initial rapid decay superimposed upon the longer decay. These effects depend upon pulse spacings but not in an understandable manner. Because T_2 does not lend itself to unambiguous interpretation but does show qualitative agreement with activated motional processes at lower temperatures, it has been included only to show that motional effects dominate the relaxation pattern at those temperatures.

CHAPTER VIII. CONCLUSIONS

The proton spin-lattice relaxation time measurements have proved to give interesting insight into the tantalum-hydrogen system. The measurements yield information on the electronic properties, the motional processes in the high temperature α phase, the differences in the diffusion rates between the phases, and the existence of certain phase boundaries.

In the high temperature α phase, both the electron spin-nuclear spin contact interaction and the motion of the hydrogen contribute to the net relaxation time. A computer fit separated the two processes. The result for the electronic contribution indicated the number of electrons at the Fermi energy decreased with increasing hydrogen content, in agreement with previous susceptibility data. The activation energy measured for hydrogen diffusion in the α phase was 0.1396 ± 0.0019 eV/atom, and this did not vary throughout the concentration range studied ($0.155 \leq H/Ta \leq 0.677$). This agrees with the low concentration data from other methods which give 0.140 eV/atom. Extrapolation of the motional contribution to the known value of the minima results in a constant temperature at the minimum through the concentration range, indicating that the value of the jump rate does not change with composition.

The measurements indicate that the α, ϵ, and ordered phases have different hydrogen jump rates. Hence, phase boundaries and two-phase regions are also detected by pulsed NMR measurements. The transitions were directly compared to the work of Schober and Carl (8) as well as to DTA results on the samples used for this study. Excellent agreement was

found between the three measurements. Additionally, the study confirms the two-phase nature of the $\alpha+\epsilon$ region and the single-phase nature of the ϵ region, both of which were reported by Schober and Carl for the first time.

From the temperatures of the minima measured or extracted from the data in this experiment, the jump rates (the inverse of the correlation time) decreased by a factor of approximately 7.2 from the α phase to the ordered phases. Although the data for the ϵ phase is limited, it appears that the diffusion is slightly slower in the ϵ phase than in the ordered phases.

In the lowest temperature region studied ($77\ K \leq T \leq 200\ K$), the spin-lattice relaxation time remains constant independent of temperature until, in the vicinity of 77 K, the relaxation time again rises with decreasing temperature. Two models were proposed to account for this anomaly. The first assumes that the hydrogen diffusional jump path involves an intermediate metastable state. This would produce two spectral density functions and could be made to fit the data presented. Alternatively, one could assume that the ^{181}Ta quadrupole levels interact with the hydrogen nuclei in such a way as to produce the anomalous region. Both models are partially supported by the data, but neither can be unequivocally substantiated because of the lack of data below 77 K and because the ^{181}Ta resonance has not been successfully measured in this system.

LITERATURE CITED

1. J. Völkl and G. Alefeld, in Diffusion in Solids, edited by A. S. Nowick and J. J. Burton (Academic Press, New York, 1975).

2. G. G. Libowitz, in Inorganic Chemistry Series One 10, edited by L. E. J. Roberts (Butterworths, London, 1972).

3. D. Zamir, Physical Review A 140, 271 (1965).

4. P. Pattison, M. Cooper, and J. R. Schneider, Zeitschrift für Physik B 25, 155 (1976).

5. J. Hauk and H. J. Schenk, Journal of the Less-Common Metals 51, 251 (1977).

6. A. C. Switendick, in Hydrogen Energy, Part B, edited by T. N. Veziroglu (Plenum, New York, 1975).

7. T. Schober and H. Wenzl, in Hydrogen in Metals, edited by G. Alefeld and J. Völkl (Springer-Verlag, Berlin, 1977).

8. T. Schober and A. Carl, Scripta Metallurgica 11, 397 (1977).

9. V. A. Somenkov, A. V. Gurskaya, M. G. Zemlyanov, M. E. Kost, N. A. Chernoplekov, and A. A. Chertkov, Soviet Physics-Solid State 10, 2123 (1969).

10. D. Slodtfelt-Ellingston and B. Pedersen, Physica Status Solidi (a) 25, 115 (1974).

11. T. Schober and H. Wenzl, Scripta Metallurgica 10, 819 (1976).

12. K. P. Roenker, R. G. Barnes, and H. R. Brooker, Berichte der Bunsengesellschaft für Physikalische Chemie 80, 470 (1976).

13a. T. Schober and U. Linke, Journal of the Less-Common Metals 44, 63 (1976).

13b. H. Asano, Y. Ishino, R. Yamada, and M. Hirabayashi, Journal of Solid State Chemistry 15, 45 (1975).

14. V. F. Petrunin, V. A. Somenkov, S. Sh. Shil'shtein, and A. A. Chertkov, Soviet Physics-Crystallography 15, 137 (1970).

15. V. A. Somenkov, A. Yu. Chervyakov, S. Sh. Shil'shtein, and A. A. Chertkov, Soviet Physics-Crystallography 17, 274 (1972).

16. H. Asano, R. Yamada, and M. Hirabayashi, Transactions of the Japan Institute of Metals 18, 155 (1977).

17. V. A. Somenkov, Berichte der Bunsengesellschaft für Physikalische Chemie 76, 733 (1972).

18. R. Hiebel and H. Wollenberger, Scripta Metallurgica 10, 945 (1976).

19. R. E. Reed-Hill, Physical Metallurgy Principles, 2nd ed. (D. Van Nostrand, New York, 1973).

20. N. Bloembergen, E. M. Purcell, and R. V. Pound, Physical Review 73, 679 (1948).

21. H. C. Torrey, Physical Review 96, 690 (1954).

22. A. Abragam, The Principles of Nuclear Magnetism (Clarendon Press, Oxford, England, 1961).

23. D. N. Beshers, University of California Lawrence Radiation Laboratory Report UCRL-7184, 1 (1964).

24. T. C. Farrar and E. D. Becker, Pulse and Fourier Transform NMR (Academic Press, New York, 1971).

25. C. P. Slichter, Principles of Magnetic Resonance (Harper and Row, New York, 1963).

26. L. I. Schiff, Quantum Mechanics, 3rd ed. (McGraw-Hill, New York, 1968).

27. J. Korringa, Physica 16, 601 (1950).

28. J. D. Will, "Nuclear Spin Relaxation of Hydrogen in Thorium Hydrides", Ph.D. Thesis, Iowa State University, Ames, 1968 (unpublished).

29. D. F. Holcomb and R. E. Norberg, Physical Review 98, 1074 (1955).

30. R. M. Cotts, Berichte der Bunsengesellschaft für Physikalische Chemie 76, 761 (1972).

31. M. Mehring, NMR: Basic Principles and Progress 11 (Springer-Verlag, Berlin, 1976).

32. E. L. Hahn, Physical Review 80, 580 (1950).

33. H. Y. Carr and E. M. Purcell, Physical Review 94, 630 (1954).

34. S. Meiboom and D. Gill, Review of Scientific Instruments 29, 688 (1958).

35. R. L. Vold, R. R. Vold, and H. E. Simon, Journal of Magnetic Resonance 11, 283 (1973).

36. P. R. Bevington, Data Reduction and Error Analysis for the Physical Sciences (McGraw-Hill, New York, 1969).

37. T. G. Berlincourt and P. W. Bickel, Physical Review B 2, 4838 (1970).

38. J. L. Conway and R. M. Cotts, Review of Scientific Instruments 48, 656 (1977).

39. D. J. Adduci, P. A. Hornung, and D. R. Torgeson, Review of Scientific Instruments 48, 661 (1977).

40. I. J. Lowe and C. E. Tarr, Journal of Physics E 1, 320 (1968).

41. A. M. Gottlieb, V. C. Srivastava, and P. Heller, Review of Scientific Instruments 43, 676 (1972).

42. D. J. Adduci, P. A. Hornung, and D. R. Torgeson, Review of Scientific Instruments 47, 1503 (1976).

43. H. Lutgemeier, R. R. Arons, and H. G. Bohn, Journal of Magnetic Resonance 8, 74 (1972).

44. B. Pedersen, T. Krogdahl, and O. E. Stokkeland, Journal of Chemical Physics 42, 74 (1965).

45. D. Zamir and R. M. Cotts, Physical Review 134, A666 (1964).

46. S. Kazama, and Y. Fukai, Journal of Less-Common Metals 53, 25 (1977).

47. Y. Fukai and S. Kazama, Acta Metallurgica 25, 59 (1977).

48. B. Stalinski, Bulletin De L'Academie Polonaise Des Sciences Cl. III 21, 245 (1954).

49. F. Ducastelle, R. Caudron, and P. Costa, Journal of the Physics and Chemistry of Solids 31, 1247 (1970).

50. I. J. Lowe and D. Tse, Physical Review 166, 279 (1968).

51. F. M. Lurie and C. P. Slichter, Physical Review 133, A1108 (1964).

52. R. C. Wayne and R. M. Cotts, Physical Review 151, 264 (1966).

ACKNOWLEDGEMENTS

The author would like to thank Dr. Richard G. Barnes for the suggestion of this topic, and for his assistance and patience throughout the course of this work.

Thanks are also extended to Dr. A. S. Khan for providing the Ta-H samples; to A. Johnson and Dr. D. T. Peterson of the Metallurgy Division of the Ames Laboratory for analyzing their hydrogen content; to Doug Adduci, John Erickson, B. F. Carter, and Harold Skank of the Ames Laboratory Instrumentation Group for their help with the apparatus and computer; to Steve Berg, a summer trainee, for his assistance with the measurements; to Len Moon for help with the software. Special thanks are due Dave Torgeson for his help with the design, construction, maintenance, and use of the spectrometer, and whose good humor and encouragement contributed much to the success of this project.

Finally, I would like to thank my wife and typist whose patience, understanding, and skill have been very helpful.